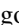





Effect of a flight stream on subsonic turbulent jetsIgor A. Maia ¹, Guillaume Brès ², Lutz Lesshafft ³, and Peter Jordan ¹¹*Prime Institute, CNRS, Université de Poitiers, ENSMA, Poitiers 86360, France*²*Cascade Technologies Inc., Palo Alto, California 94303, USA*³*Laboratoire d'Hydrodynamique, CNRS–Ecole Polytechnique, Palaiseau 91120, France*

(Received 20 January 2023; accepted 16 May 2023; published 6 June 2023)

This study concerns a turbulent jet at Mach number $M_j = 0.9$, subject to a uniform external flow stream at $M_f = 0.15$. The analysis combines experimental and numerical databases, spectral proper orthogonal decomposition (SPOD), and linear modeling. The experiments involve time-resolved, stereo PIV measurements at different cross-sections of the jet. A companion large-eddy simulation was performed with the same operating conditions using the “CharLES” solver by Cascade Technologies to obtain a complete and highly resolved three-dimensional database. We assess the mechanisms that underpin the reduction in fluctuation energy that is known to occur when a jet is surrounded by a flight stream. We show that this energy reduction is spread over a broad region of the frequency-wave-number space and involves, apart from the known stabilization of the modal Kelvin-Helmholtz (KH) instability, the attenuation of flow structures associated with the nonmodal Orr and lift-up mechanisms. Streaky structures, associated with helical azimuthal wave numbers and very slow timescales, are the most strongly affected by the flight stream, in terms of energy attenuation and spatial distortion. The energy reductions are accompanied by a weakening of the low-rank behavior of the jet dynamics. These trends are found to be consistent, to a great extent, with results of a local linear model based on the modified mean flow in the flight-stream case.

DOI: [10.1103/PhysRevFluids.8.063902](https://doi.org/10.1103/PhysRevFluids.8.063902)**I. INTRODUCTION**

Recent research on turbulent shear flows has been driven by a need to obtain simplified descriptions of flow dynamics that would reduce the Navier-Stokes system to a form adapted to describe a subspace of essential mechanisms, with respect to an observable of interest (drag, momentum, noise, etc.). Such mechanisms are often associated with large-scale (with respect to turbulence integral scales) organized motion in the form of coherent structures. It is their widespread presence in turbulent flows [1] that motivates the development of simplified models.

Coherent structures are easily identifiable in unstable laminar flows, where the exponential growth of small disturbances underpins transition to turbulence. In that case, they can be modeled as instability waves using linear stability theory, where linearization is performed about the laminar base state. In the turbulent regime, organized motion often persists and early observations in mixing layers [2] and jets [3] revealed a remarkable resemblance with linear instability mechanisms found at lower Reynolds numbers. Eduction of coherent structures in high-Reynolds-number, turbulent jets, is challenging on account of their low fluctuation energy and their stochastic space-time organization. That is why early attempts to study coherent structures in jets relied on external periodic forcing, which raises the coherent-structure energy above the background level and enhances their organization [4–9].

More recently, there has been considerable progress in the identification and modeling of coherent structures in unforced jets, thanks to progress in experimental techniques, the use of

advanced signal processing approaches such as proper orthogonal decomposition (POD) [10] and spectral proper orthogonal decomposition (SPOD), and linear mean-flow modeling. For instance, Kelvin-Helmholtz (KH) type wavepackets have been identified in the hydrodynamic pressure near-field [11–13] and in the velocity field [14,15] of unforced turbulent jets. The experimentally deduced wavepackets are found to be in good agreement with solutions to the parabolized stability equations (PSE) in the initial jet region for azimuthal wave numbers $m = 0, 1, 2$ and frequencies in the range $0.3 \leq St \leq 1$, where $St = fU_j/D$ is the Strouhal number (with f being the frequency, U_j the jet exit velocity, and D the nozzle diameter). Later, Sasaki *et al.* [16] showed, using large-eddy simulation data, that agreement persists for Strouhal numbers as high as $St = 4$ for the axisymmetric and first three helical azimuthal wave numbers.

The above studies show compelling evidence for the existence of modal convective instability mechanisms in jets. More recently, attention has been turned to nonmodal linear mechanisms, such as the Orr [17] and lift-up [18] mechanisms, that give rise to different flow structures. These mechanisms, known to be important in the dynamics of wall-bounded flows (see the reviews by Brandt and Jiménez [18,19]), were also observed in early experiments in jets [20–24]. Recent studies have shown that they are dominant at very low Strouhal numbers, and their most salient features can be modeled through linear mean-flow analysis [25–32].

There is now a well-documented body of work concerning modal and nonmodal mechanisms in jets, and linear mean-flow analysis provides a valuable framework for understanding the dynamics of coherent structures associated with these mechanisms, and eventually estimating and controlling them. One important caveat needs to be mentioned, though: the validity of linear mean-flow analysis must be demonstrated *a posteriori*, since the flow linearization procedure does not result in an exact equation [33], and there is no guarantee that the same models will hold under different flow configurations. Turbulent jets in the presence of a flight stream, which are the focus of this work, are one example of a flow configuration for which the validity of linear mean-flow models needs to be explored through comparisons with data.

A. Jets with flight stream

Jets subject to a uniform external flight stream are a flow configuration of interest to the aeronautic industry, as it mimics the effect of forward flight in real aircraft. It is known that a flight stream modifies the mean flow development, producing a stretching of the potential core, reduction of the shear-layer thickness, turbulent kinetic energy, and a reduction of the associated radiated sound levels [34]. Such mean-flow modifications have a stabilizing effect on the modal KH mechanism, as shown by Michalke *et al.* [35], with an inviscid locally parallel stability analysis. More recently, Soares *et al.* [36] extended the analysis by taking into account the jet mean-flow divergence in a PSE formulation. The results confirm a reduction in wavepacket growth rates with increasing flight-stream velocity, followed by an increase in their convection velocity. The dynamics of axisymmetric wavepackets in the presence of a coflow have also been studied by Garnaud *et al.* [37] using a global resolvent analysis. The flow response modes (both in the near-field and the far-field) were found to be in good qualitative agreement with (nonlinear) flow data, thus confirming that the linear-mean-flow framework can capture the effect of flight on axisymmetric coherent structures associated with modal growth mechanisms in jets.

Most studies on the effect of a flight stream on turbulent jets have focused on sound-radiation aspects [38–45]. In this work we characterize the effect of a flight stream on the turbulent flow field of a subsonic jet. As discussed above, there is now an extensive characterization in the literature of modal and nonmodal linear mechanisms in jets in “static” conditions. And although the effect of the flight stream on the KH instability has been studied [35,36], to the best of our knowledge no studies so far have characterized the changes in nonmodal linear instability mechanisms (Orr and lift-up) in flight conditions. Indeed, there has not yet been a demonstration that linear mean-flow-models can correctly capture the effect of flight on coherent structures associated with nonmodal mechanisms. This is what motivates the present work. Figure 1 shows spectra of acoustic pressure measured at

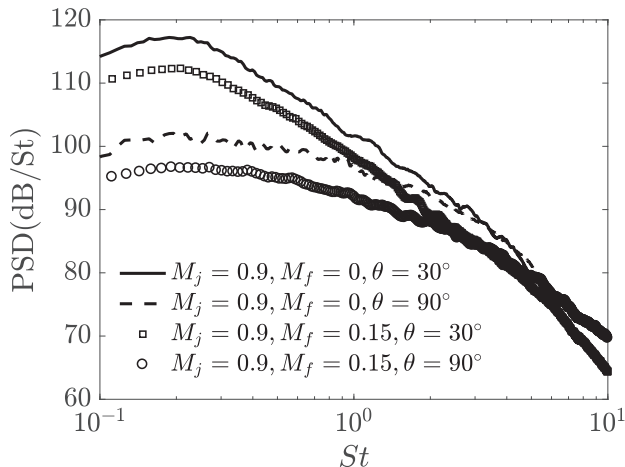


FIG. 1. Power spectral densities (PSD) of pressure measured in the acoustic field of jets with and without flight stream at polar angles of $\theta = 30^\circ$ and $\theta = 90^\circ$ from the jet axis. St stands for Strouhal number.

polar angles of $\theta = 30^\circ$ and $\theta = 90^\circ$ from the jet axis, in the setup described in Sec. II. The flight stream is seen to produce an effect at both angles for a broad range of Strouhal numbers, as a consequence of changes to the turbulent field. At low frequencies and small angles from the jet axis, represented here by $\theta = 30^\circ$, the main sound-producing mechanism is associated with axisymmetric ($m = 0$) jittering KH wavepackets [46–48]. At sideline, higher azimuthal wave numbers become dominant [47]. The observed reduction in sound pressure levels (SPL) in the presence of the flight stream is consistent with Lighthill’s eighth power law [49] if we consider the centerline-to-freestream velocity difference, $dU = U_j - U_\infty$, as a characteristic flow velocity. dU reduces from 0.9 to 0.75 with the flight stream. From Lighthill’s law, the acoustic power should be reduced by a factor of $10\log_{10}[(0.75/0.9)^8] = -6.33$ dB. For measurements taken at the same distance for both flow conditions, this translates into the same difference in SPL, and is close to what is reported in Fig. 1, for both measurement angles.¹ However, Lighthill’s law does not reveal the details of how the change in turbulent kinetic energy is organized in the frequency-wave-number spectrum, or how it affects the dynamics of coherent structures which are likely associated with those changes. A thorough characterization of frequency-wave-number spectra with and without the flight stream is a key aspect of this study, and we will be interested in exploring to what degree the changes in the spectrum of turbulent velocity fluctuations can be associated with changes in the aforesaid categories of coherent structures.

In the case of a laminar jet, linear, fixed-point analysis of the effect of flight stream could be expected to reveal an attenuation of all shear-driven linear instability mechanisms, because of the reduction of shear that is produced by the flight stream. However, for fully turbulent jets, as mentioned above, it is not clear *a priori* whether changes in the energy spectrum are associated with linear or nonlinear mechanisms. A direct connection between the flight stream and changes in coherent structures associated with linear mechanisms is therefore much less clear. A central objective of the present work is, therefore, in addition to an extensive characterization of the changes produced by a flight stream, to explore the extent to which the observed changes can be explained by linear mean-flow mechanisms.

¹We are grateful to an anonymous reviewer for pointing out the consistency with Lighthill’s eighth power law.

Our analysis combines experimental and numerical databases, modal decomposition and locally parallel, linear mean-flow analysis. The experiments were performed at the Pprime Institute and consisted of time-resolved (TR), stereo PIV measurements at different cross-sections of a jet at Mach number $M_j = 0.9$ subject to a uniform external flight stream at $M_f = 0.15$. Throughout the paper, the database is systematically compared to a case with no flight stream, $M_f = 0$. Companion LES databases were generated for the same operating conditions using the “CharLES” solver by Cascade Technologies [50,51] to obtain a high-fidelity 3D database, allowing us to perform global SPOD.

The remainder of the paper is organized as follows: in Sec. II we describe the experimental setup and provide details about flow conditions and PIV treatment. This is followed by a description of the numerical setup in Sec. III. In Sec. IV we show the effect of the flight stream on first-order statistics and relevant mean-flow quantities. This part consists in a validation of the two databases with respect to previously reported results. In Secs. V and VI the effect of the flight stream is investigated in more depth through Fourier decompositions and local SPOD. Results of a local mean-flow model are presented in Sec. VII and interpreted in light of the PIV data. Global SPOD analysis using the LES data is discussed in Sec. VIII, and finally some concluding remarks are given in Sec. IX.

II. EXPERIMENTAL SETUP

The experiments were performed at the Bruit & Vent jet facility of the Pprime Institute in Poitiers, France. We performed measurements in jets at Mach number of $M_j = U_j/c_\infty = 0.9$, where U_j is the jet exit velocity and c_∞ the ambient speed of sound. The corresponding Reynolds number was $Re = U_j D/\nu = 1 \times 10^6$, where ν is the kinematic viscosity and D is the nozzle diameter, which was 50 mm. The jet was subject to an external uniform stream which could attain a maximum Mach number of $M_f = U_f/c_\infty = 0.15$, where U_f is its exit velocity. The flight stream comes from an outer convergent section that surrounds the main nozzle and finishes in a straight section of diameter 600 mm. The operating conditions in terms of nozzle-pressure ratio are $NPR = P_{t_j}/P_\infty = 1.7$ for the main jet and $NPR = P_{t_f}/P_\infty = 1.006$ for the flight stream, with P_{t_j} the total pressure and P_∞ the ambient pressure. The experiments were performed in isothermal conditions, the static temperatures of the main jet and the flight stream being controlled to ensure this. The internal and external boundary layers were tripped so as to produce turbulence, similar to what was done in previous studies in static conditions [51], at 3D upstream of the nozzle exit.

We performed a series of low-frequency-2D and time-resolved (TR), stereo-PIV measurements. The former were used to characterize the effect of the flight stream in zero and first-order statistics, such as mean-flow distortion and reduction of turbulent kinetic energy, with increasing flight-stream Mach number, varying from $M_f = 0$ to $M_f = 0.15$. In the 2D setup, the laser sheet is aligned with the jet axis, allowing a fine discretization in the streamwise direction. The setup consisted of two Lavision Imager LX cameras and a Quantel Evergreen 532 nm, 200 mJ laser. The images had a resolution of 4920×3280 pixels, which allowed us to cover an x - y plane in the range $x \in [0.15D, 10D]$ $y \in [-1.9D, 1.9D]$, resulting in one vector every $0.009D$. A total of 10 000 PIV images were acquired at a rate of 4 Hz, which was found to be sufficient to converge mean and root-mean-square (rms) fields. Both the main jet and the flight stream were seeded with glycerine smoke particles with diameters in the range 1–2 μm , similar to what was done in previous PIV campaigns [15]. These experiments were used to characterize velocity statistics with four different flight-stream levels corresponding to $M_f = 0, 0.05, 0.1, 0.15$.

The characterization of different instability mechanisms requires time-resolved flow data decomposed in azimuthal Fourier modes. This was achieved with the stereo TR-PIV setup, which featured two Photron SAZ cameras and a 532 nm, 2×60 W continuum Mesa laser. The cameras were positioned in a forward scattering configuration, to assure maximal light intensities. The angle formed by the cameras and the laser sheet was 45° (with both cameras on the same side of the laser source), and Scheimpflug adaptors were used to ensure a correct focus on the entirety of the field of view. A resolution of 1024×1024 pixels was used to focus on a field of view in the range

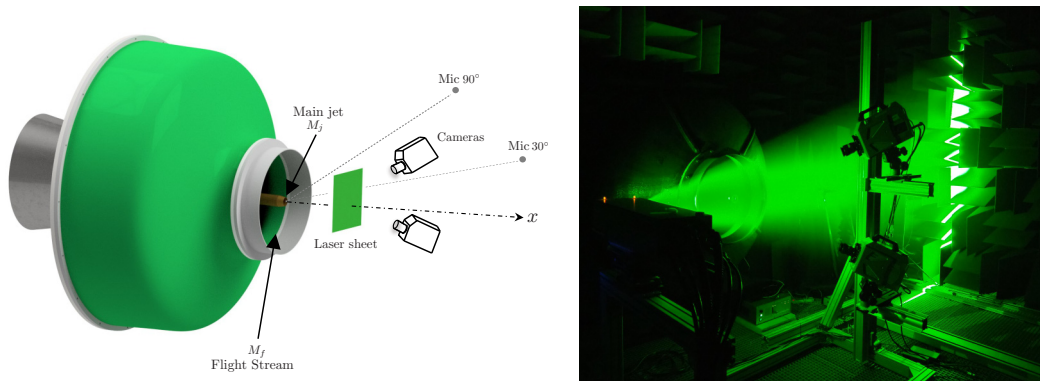


FIG. 2. Schematic of the jet facility showing the main elements of the stereo PIV system, along with a picture of the experiment setup in the wind tunnel.

$y \in [-1D, 1D]$, $z \in [-1D, 1D]$, resulting in one vector every $0.026D$. The image acquisition was performed in double frame mode at a frequency of 10 kHz, corresponding to a Strouhal number of $St = fU_j/D = 1.6$, giving a total of 21 000 images per plane measured. The laser sheet had a thickness of 3 mm, and the time between laser pulses was set to $2.5 \mu\text{s}$, resulting in a maximum displacement of 4 pixels across the laser sheet. For both the 2D and TR-stereo configurations, PIV computations were carried out using a commercial software which performed a multi-pass iterative PIV algorithm [52]. The PIV interrogation area size was set to 64×64 pixels for the first pass, decreased to 16×16 pixels with an overlap of 50 between two neighboring interrogation areas. Each instantaneous snapshot was interpolated into a polar grid, r - θ using a bicubic interpolation to perform a Fourier decomposition in azimuth [15]. The measurements in the TR-stereo configuration were carried out for two flight-stream conditions, $M_f = 0$ and $M_f = 0.15$, the same used in the numerical databases. Several PIV planes were measured in both conditions at different streamwise stations ranging from $x/x_c = 0.04$ to $x/x_c = 2$, where x_c is the potential core length.

Figure 2 shows a schematic of the jet facility and the TR-PIV setup along with a picture of the setup in the wind tunnel. A summary of the operating conditions of the experiments are shown in Table I. Acoustic measurements were performed (in the absence of the PIV setup) at polar angles of 30° and 90° to the jet axis, at a distance of $50D$ from the nozzle. Acoustic data was sampled at a rate of $St_s = 32.7$ for 30 s. PSDs reported in Fig. 1 were computed with Welch's method, using 5860 blocks with 50% overlap. Complementary Pitot tube and hot-wire measurements were performed for case 4 to characterize the boundary layers, and are described in more detail in Sec. IV.

TABLE I. Operating conditions and experimental parameters of the experiments. The last two columns indicate which kind of PIV setup was used for each condition.

Case	Re	M_j	M_f	T_j/T_f	2D-PIV	TR-stereo PIV
1	10^6	0.9	0	1	✓	✓
2	10^6	0.9	0.05	1	✓	–
3	10^6	0.9	0.10	1	✓	–
4	10^6	0.9	0.15	1	✓	✓

TABLE II. Operating conditions and simulation parameters of the main LES, where t_{sim} is the simulation time and Δt is the sampling period of the database recording.

Case name	Mesh size	M_j	M_f	T_j/T_f	Re	dtc/D	$\Delta tc/D$	$t_{\text{sim}}c/D$
<i>BL16M_M09</i>	15.9×10^6	0.9	0	1.0	1×10^6	0.001	0.1	3000
<i>BL22M_M09_Mf015</i>	21.8×10^6	0.9	0.15	1.0	1×10^6	0.001	0.1	2000

III. NUMERICAL SETUP

To complement the experiments, the jet configurations with and without flight stream are investigated with high-fidelity large eddy simulations using the compressible flow solver ‘‘CharLES’’ developed at Cascade Technologies [50]. Results for the isothermal Mach 0.9 turbulent jet issued from the contoured convergent-straight nozzle of exit diameter $D = 50$ mm at $M_f = 0$ were initially reported by Brès *et al.* [51]. The present work is an extension of the study for both $M_f = 0$ and 0.15 with longer databases and higher sampling frequency. All the large eddy simulations feature localized adaptive mesh refinement, synthetic turbulence and wall modeling on the internal nozzle surface (and external nozzle surfaces at $M_f = 0.15$) to match the fully turbulent nozzle-exit boundary layers in the experiments. The LES methodologies, numerical setup and comparisons with measurements are described in more details in Brès *et al.* [51] and are only briefly summarized here.

The round nozzle geometry [with exit centered at $(0, 0, 0)$] is explicitly included in the axisymmetric computational domain, which extends from approximately $-10D$ to $50D$ in the streamwise (x) direction and flares in the radial direction from $20D$ to $40D$. The uniform external flight stream is imposed as upstream boundary condition outside the nozzle in the simulation. Note that a very slow coflow at Mach 0.009 is used in the LES at no flight-stream condition to prevent any spurious recirculation and facilitate flow entrainment. Sponge layers and damping functions are applied to avoid spurious reflections at the boundary of the computational domain [53,54]. The Vreman [55] subgrid model is used to account for the physical effects of the unresolved turbulence on the resolved flow.

The nozzle pressure ratio and nozzle temperature ratio are $\text{NPR} = P_t/P_f = 1.7$ and $\text{NTR} = T_t/T_f = 1.15$, respectively, and match the experimental conditions. The jet is isothermal ($T_j/T_f = 1.0$), and the jet Mach number is $M_j = U_j/c = 0.9$. For both experiment and simulation, the Reynolds number is $\text{Re} = \rho_j U_j D / \mu_j \approx 1 \times 10^6$.

In the experiment, transition is forced using a sandpaper strip located approximately $3D$ upstream of the nozzle exit plane on the internal nozzle surface for all configurations, and on the external nozzle surface for $M_f = 0.15$. In the LES, synthetic turbulence boundary conditions are used to model these experimental boundary layer trips present on the internal and external nozzle surfaces. To properly capture the internal and external turbulent boundary layers, localized isotropic mesh refinement and wall modeling [56,57] are applied on the interior and exterior surface from the boundary layer trip to the nozzle exit. All the other solid surfaces are treated as no-slip adiabatic walls. While several meshes were considered as part of a grid resolution study [51], the standard unstructured mesh containing approximately 16 million control volumes is used for the present work with $M_f = 0$, and the case is simply referred to as *BL16M_M09* (i.e., extension of case *BL16M_WM_Turb* from [51]). For $M_f = 0.15$, the same isotropic near-wall mesh refinement used to capture the boundary layer inside the nozzle is applied outside of the nozzle. The mesh size is therefore increased to approximately 22 million control volumes, and the case is referred to as *BL22M_M09_Mf015*.

Table II lists the simulation parameters and settings for the LES runs with and without flight stream, including the time step dt , the total simulation time t_{sim} for the collection of statistics and data (after the initial transient is removed), and the sampling period Δt for the recording for the main LES databases. Note that the sampling period for the recording of the FW-H surface data for far-field noise predictions is $0.5\Delta t$.

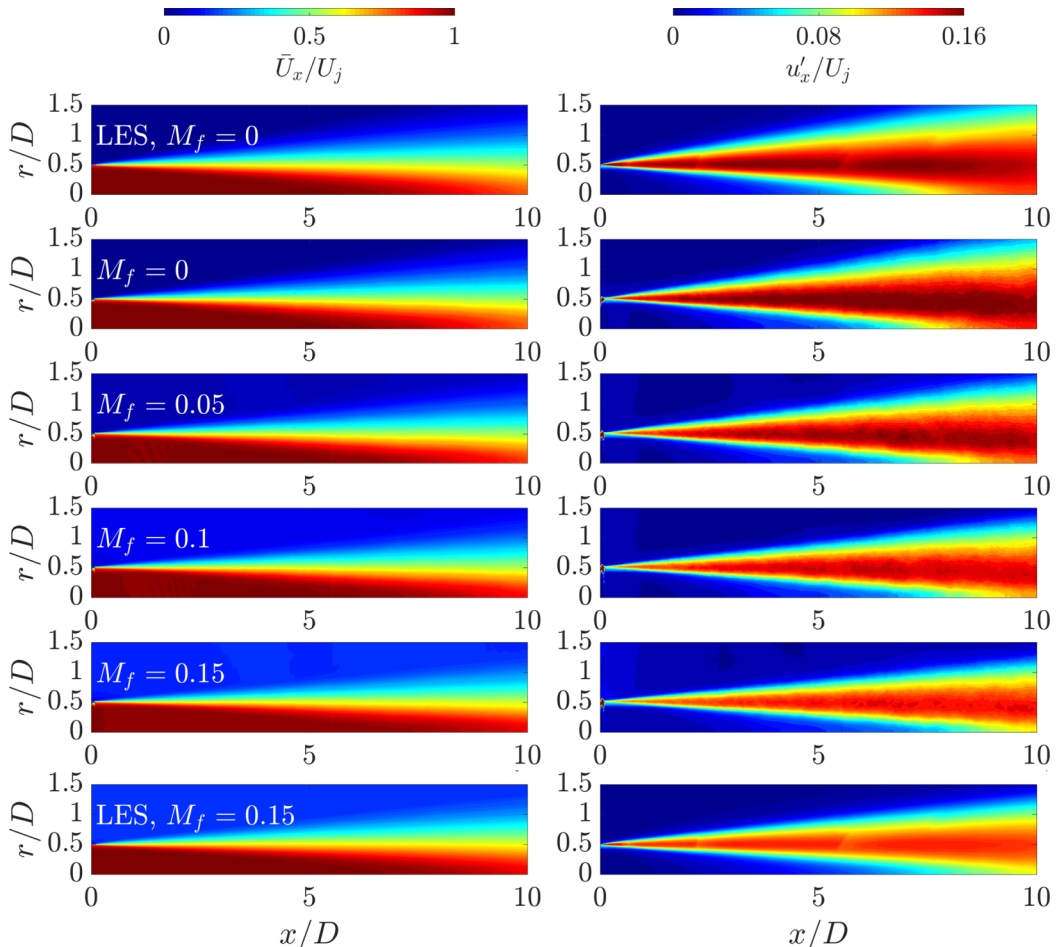


FIG. 3. Contours of mean, \bar{U}_x (left), and rms, u'_x (right), streamwise velocity for jets at $M_j = 0.9$ and different flight-stream Mach numbers. Velocities are normalized by U_j . The first and last contour maps correspond to LES data, and the intermediary ones to PIV results.

To facilitate postprocessing and analysis, the LES data is interpolated from the original unstructured LES grid onto structured cylindrical grids in the jet plume and in the nozzle pipe. These structured cylindrical grids were originally designed for the grid with 16M control volumes, such that the resolution approximately corresponds to the underlying LES resolution. For both structured grids, the points are equally spaced in the azimuthal direction to enable simple azimuthal decomposition in Fourier space.

IV. ZERO- AND FIRST-ORDER STATISTICS

We start with an analysis of the effect of the flight stream on zero- and first-order velocity statistics, to provide a validation of the experimental and numerical databases. It is known that a flight-stream affects the jet development by lengthening the potential core and reducing shear-layer spreading and turbulence intensities [34]. These trends can be seen in Fig. 3, which presents contour plots of mean and rms streamwise velocity on a meridional plane, measured with the 2D-PIV setup, with increasing M_f . LES data for the case $M_j = 0.9$, $M_f = 0.15$ is also shown for comparison.

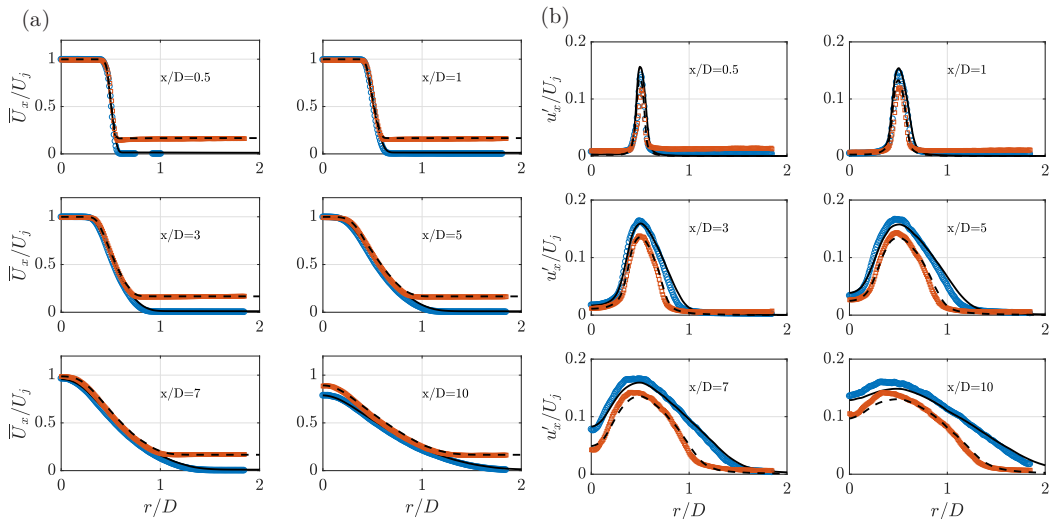


FIG. 4. Comparison between experimental and numerical mean (a) and rms (b) radial profiles of streamwise velocity component at different streamwise positions. \circ : exp. $M_f = 0$; \square : exp. $M_f = 0.15$; —:LES data for $M_f = 0$, *BL16M_M09*; - - -: LES data for $M_f = 0.15$, *BL22M_M09_Mf015*.

The LES and experimental databases were found to be in excellent agreement, as can be seen in the radial profiles of mean and rms velocities shown in Fig. 4 for different streamwise positions. LES data for the no-flight case, *BL16M_M09*, is also shown for comparison. Both jets exhibit a classic change from top-hat profiles in the near-nozzle region to bell-shaped profiles further downstream. However, the reduction in shear-layer thickness becomes apparent after a couple of jet diameters with increasing M_f . The rms profiles measured in the presence of the flight stream show amplitude reductions throughout the jet. These reductions are concentrated in radial positions around the peak in the initial jet region, but spread across the shear layer further downstream.

The mean-flow shape changes with increasing flight-stream levels. We assessed three important flow features at different conditions of flight-stream Mach number, M_f : the potential core length, x_c , defined here as the streamwise position where $\tilde{U}_x(x, 0) = 0.95U_j$, the centerline velocity decay and the shear-layer momentum thickness, δ_θ , defined as

$$\delta_\theta(x) = \int_0^{r_{0.05}} \frac{\tilde{U}_x(x, r)}{\tilde{U}_x(x, 0)} \left(1 - \frac{\tilde{U}_x(x, r)}{\tilde{U}_x(x, 0)} \right) dr, \quad (1)$$

where \tilde{U}_x is a normalized mean flow velocity,

$$\tilde{U}_x(x, r) = \frac{\tilde{U}_x(x, r) - U_f}{\tilde{U}_x(x, 0) - U_f}. \quad (2)$$

The evolution of these quantities with increasing M_f is shown in Fig. 5. The potential core length grows approximately linearly with M_f in the range of conditions tested, presenting an increase of 17% between the no-flight-case and the case with $M_f = 0.15$. The jet development is also affected downstream of the potential core, where the velocity decays at smaller rates in the presence of the flight stream. This delayed development is also manifest in momentum thicknesses, which are significantly reduced. Figures 5(d) and 5(e) show the evolution of centerline velocity and momentum thickness with the streamwise coordinate scaled by the case-dependent core length x_c . It can be seen that this scaling produces a collapse of the centerline velocity decay. The momentum thickness, however, does not collapse so well with this scaling, and the shear layer remains thinner in the flight case, even when the flow stretching is taken into account.

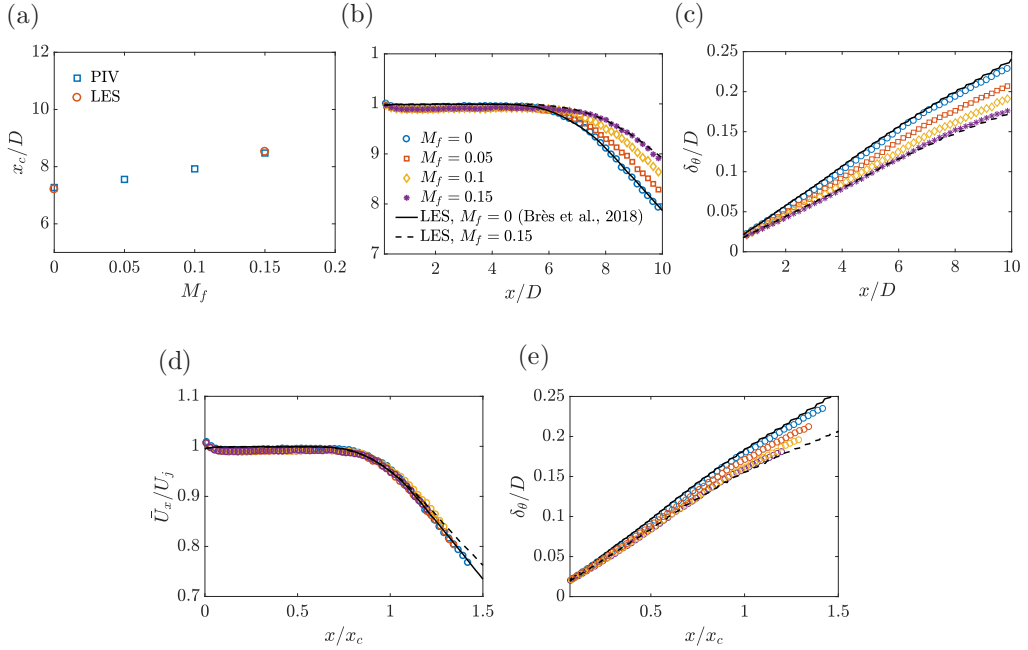


FIG. 5. Variation of mean-flow quantities with increasing flight-stream velocity for a jet at $M_j = 0.9$. (a) Potential core length; (b) centerline velocity decay; (c) streamwise evolution of the momentum thickness. Panels (d) and (e) show centerline velocity and momentum thickness profiles when the streamwise coordinate is scaled by potential core length, x_c . Legends in panels (c)–(e) are the same as in panel (b).

The boundary layer, which is now recognized as an important flow region underpinning jet dynamics and sound radiation [30,51,58] was also characterized through Pitot tube and hot-wire measurements. Figure 6 shows mean and rms profiles for the flight-stream case measured at $x/D = 0.0024$, which was the closest position attainable without damaging the probes. The hot-wire

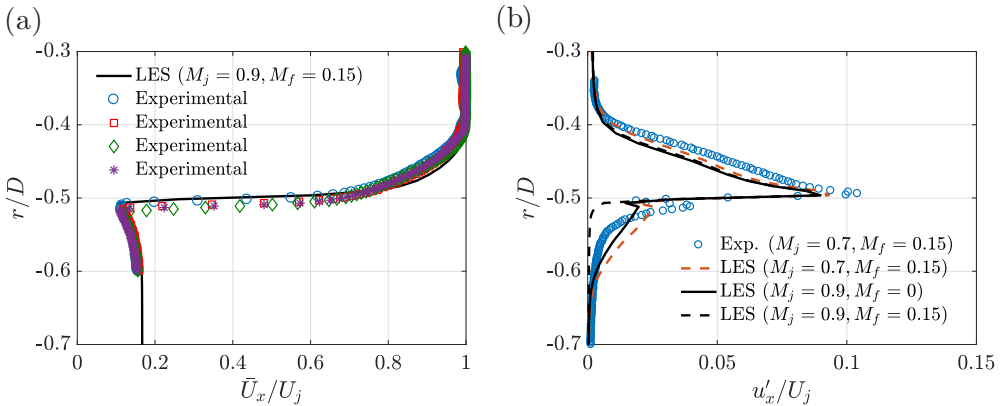


FIG. 6. Nozzle-exit mean (a) and rms (b) boundary layer profiles of streamwise velocity, measured in the flight-stream case, $M_f = 0.15$. The different experimental profiles in panel (a) correspond to measurements performed at different azimuthal positions, showing the homogeneity of the boundary layer. Rms profiles for the static case, $M_f = 0$, are shown in panel (b) for comparison.

had a length of 1.25 mm and a diameter of 2.5 μm , and the measurements were performed with a 55M01 Dantec anemometer at a frequency of 30 kHz ($St = 4.8$). The homogeneity of the boundary layer was verified by measuring the profiles at different azimuthal positions, which were found to be in good agreement with each other and the LES profile. Regarding the hot-wire measurements, at $M_j = 0.9$ the *in situ* calibration of the probes was found to be very problematic, with large errors in the calibration coefficients due to compressibility effects and the large total temperature gradients in the thin initial shear layer. This issue was mitigated by performing the measurements at a lower Mach number, $M_j = 0.7$, for which there was also another LES database available. As shown in Fig. 6(b), the differences between boundary layer profiles at $M_j = 0.7$ and $M_j = 0.9$ are slight. Rms profiles from the static and flight cases are found to be quite similar in the inner part of the shear layer. In the outer part, $|r/D| > 0.5$, rms values are higher in the presence of the flight stream, as expected. A second peak is seen in the $M_f = 0.15$ profiles at $r/D \approx 0.51$, due to the external boundary layer. The LES profiles are found to be in good agreement with hot-wire data. The peak turbulence intensity and the shape of the curves are consistent with previously investigated turbulent jets.

Overall, the numerical and experimental databases for the jets at $M_j = 0.9$ and $M_f = 0$ are found to be in excellent agreement. Experimental data for the no-flight case, $M_f = 0$, agrees with previously reported data [51]. Furthermore, the trends in mean flow distortion and rms fields with the flight stream are consistent with data reported in the literature. We now proceed to a more detailed investigation of the effect of the flight stream on structures contained in the turbulent flow, which involves an analysis of energy distribution in the frequency-wave-number space.

V. ENERGY DISTRIBUTION ACROSS AZIMUTHAL MODES

We first consider the energy distribution across azimuthal wave numbers and assess how this is affected by the coflow. This is done by first interpolating the TR-PIV instantaneous fields $u(y, z, t)$ onto a polar grid $u(r, \theta, t)$ and then decomposing them into a Fourier series in θ , obtaining a field $u(r, m, t)$, with m the azimuthal wave number [14,15]. This field is then used to compute mean-squared velocity fluctuations, $u_x^2(r, m)$.

We use the potential core length, x_c as a mean-flow scaling parameter. Throughout the remainder of the study we make comparisons between the $M_f = 0$ and $M_f = 0.15$ cases at different streamwise positions on the basis of the normalized coordinate, x/x_c . In previous studies of jets subject to an external flow, attempts have been made to find “stretching factors” that, when used as a suitable scaling to the coordinate system, would make the flow field, the stability characteristics, and turbulent quantities and sound field independent of the external flow velocity. For instance, Michalke *et al.* [59] proposed a scaling factor proportional to the velocity difference which is used to model, with some degree of success, the reduction in SPL produced by the external flow. The factor is calibrated through a fitting procedure of acoustic data. In a similar spirit, Michalke *et al.* [35] has shown that a scaling can be found that accounts at the same time for the reduction of spatial growth rates of the Kelvin-Helmholtz instability and for the change in the range of unstable frequencies. The scaling factor, however, is wave-number-dependent. Here we use the potential core length as a physical scaling factor, without delving much further in the search for a “universal” scaling of all aspects of jet dynamics and sound radiation. The suitability of this choice will be discussed in light of the results shown in the following.

Figure 7 shows the distribution of energy for different m at four different positions: $x/x_c = 0.23, 0.45, 0.96, 1.6$. To provide a metric that represents the energy at each m and streamwise position, mean-squared velocities are averaged across the shear layer, in the interval $0 \leq r/D \leq 2$. Comparisons of the averaged quantity, $\langle u_x^2(m) \rangle_{\text{avg}}$, in the static and flight cases, illustrate the overall effect of the flight stream in the wave-number energy distribution at each streamwise station, independent of radial position. At streamwise locations closer to the nozzle exit, the energy distribution is quite broadband, with at least 20 azimuthal modes having significant energy relative to the peak, which occurs around $m = 7-8$ at $x/x_c = 0.23$. As one moves downstream, the distribution becomes

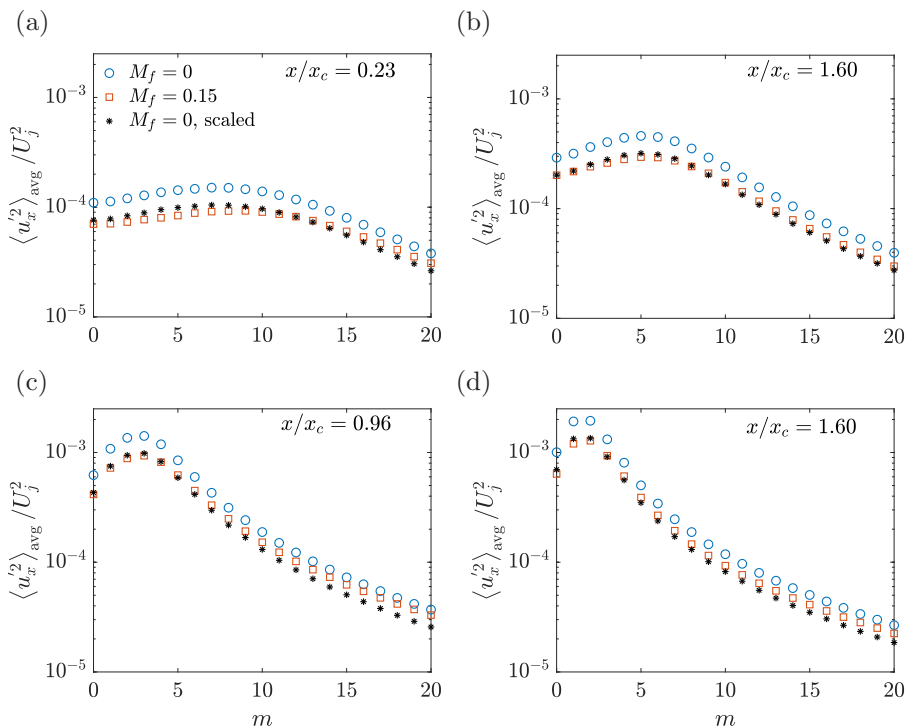


FIG. 7. Energy of streamwise velocity fluctuations integrated in r as a function of azimuthal wave number, m , for different streamwise positions, x/x_c . The black asterisks represent the energy of the static case scaled by the factor $(dU_f/dU_s)^2$, which represents the change in the centerline-to-freestream velocity in static and flight conditions.

more narrowband and the energy peak is shifted toward lower m . This is a trend that has also been observed by past experimental [14,60,61] and numerical studies [32]. Figure 7 also reveals that the flight stream produces substantial reductions in energy levels for all azimuthal wave numbers analyzed. Also shown is a rescaling of the energy of the static case by the factor $(dU_f/dU_s)^2$, which represents the reduction in the centerline-to-freestream velocity in static and flight conditions. The scaled energy falls quite close to the values of the flight case, consistent with an expected global reduction of turbulence. Notice, however, that the rescaling works better around the peak energy, and some discrepancy is seen for high azimuthal wave numbers. Notice also that at the position closest to the nozzle exit, there is a slight shift of the peak toward higher m with the flight stream.

The downstream evolution of the azimuthal wave number of the energy peak was also found to be similar, once normalized by x_c , with and without the flight stream, as seen in Fig. 8. In both cases, the peak evolves toward lower m with downstream position, approximately scaling as $\sim 1/(x/x_c)^n$. The exponent n which provides the best fit with the data was found to be virtually the same for both jets. Far downstream, past the end of the potential core, mode $m = 1$ becomes dominant in the experimental data. In the results of Figs. 7 and 8 one can note a subtle difference between near-nozzle and downstream regions. In the former, the peak wave number is different, whereas further downstream the trends are virtually identical for the two jets.

VI. FREQUENCY-WAVE-NUMBER ENERGY MAPS

We now continue the analysis by further decomposing the velocity field into Fourier modes in time. The decomposed velocity field then becomes a function of frequency (expressed by the

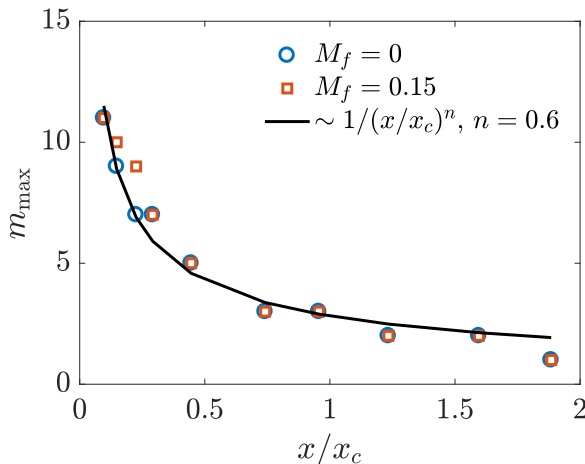


FIG. 8. Azimuthal wave number of the peak energy as a function of x/x_c . The black line is a fit of the form $1/(x/x_c)^n$ for the $M_f = 0$ and $M_f = 0.15$, respectively. $n = 0.6$ was found to provide a near-optimal fit for both cases.

Strouhal number), azimuthal wave number, and radial position, and we can assess the effect of the flight stream in the frequency-wave-number plane. Next we perform a spectral proper orthogonal decomposition (SPOD) on $\hat{u}_x(\text{St}, m, r)$. SPOD decomposes the data into an orthogonal basis ranked in terms of an energy norm. This decomposition is instructive for turbulent flows because it acts like a filter for coherent structures: their dynamics are often well represented by the leading mode and its modal energy. Leading SPOD modes can frequently be associated with the Kelvin-Helmholtz, Orr, and lift-up mechanisms, once compared with linear mean-flow analysis, according to their region of dominance in the $\text{St}-m$ plane [31,32]. It is important to emphasize, though, that a clear demarcation between the linear mechanisms in the frequency-wave-number plane does not exist. For example, in the low St range, coherent structures are likely a mixture (for non zero m) of Orr structures, streaks and weak KH wavepackets. Likewise, for the $m = 0$ mode, the change from KH to Orr-type structures with decreasing St is gradual, with no clear-cut transition. In that sense, different regions of the $\text{St}-m$ plane should be seen merely as indications of mechanism dominance, which is nonetheless useful insofar as away from the gray zones the distinction is relatively clear. With that in mind, in the following we analyze the modal energy maps of the leading SPOD mode, which in Sec. VII will be associated with instability mechanisms studied through linear mean-flow analysis.

In the framework of SPOD, given the state vector, $\mathbf{q} = [\rho, u_x, u_r, u_\theta, T]^T$, SPOD modes for a given azimuthal wave number and Strouhal number pair, $\Psi_{m,\omega}$ are obtained through eigen decomposition of the cross-spectral-density (CSD) matrix, $\hat{\mathbf{S}}_{m,\omega}$,

$$\hat{\mathbf{S}}_{m,\omega} \mathbf{W} \Psi_{m,\omega} = \Psi_{m,\omega} \Lambda_{m,\omega}. \quad (3)$$

The cross-spectral-density matrix is computed as $\hat{\mathbf{S}}_{m,\omega} = \hat{\mathbf{Q}}_{m,\omega} \hat{\mathbf{Q}}_{m,\omega}^*$, where $\hat{\mathbf{Q}}_{m,\omega} = [\hat{\mathbf{q}}_{m,\omega}^{(1)} \hat{\mathbf{q}}_{m,\omega}^{(2)} \dots \hat{\mathbf{q}}_{m,\omega}^{(N_{blk})}]$ is the ensemble of N_{blk} flow realizations at (m, ω) , with $\hat{\mathbf{q}}_{m,\omega}^{(l)}$ denoting the l th realization of the Fourier transforms in time and azimuthal direction at the frequency ω and wave number m . The eigenvalues, $[\lambda_{m,\omega}^{(1)}, \lambda_{m,\omega}^{(2)} \dots \lambda_{m,\omega}^{(N_{blk})}]$ corresponding to the modal energy are organized in decreasing order in the diagonal matrix $\Lambda_{m,\omega}$. The modes so obtained are orthogonal in a given inner product,

$$\langle \mathbf{q}_1, \mathbf{q}_2 \rangle = \mathbf{q}_1^* \mathbf{W} \mathbf{q}_2, \quad (4)$$

where \mathbf{W} is a weight matrix containing the numerical quadrature weights and choice of a given norm.

We first consider, using the experimental database, CSDs of different cross-sections of the jet. This “local” approach serves two main purposes: first, it allows us to analyze the evolution of the local organization with increasing streamwise distance; and second, it allows us to study coherent structures in the initial jet region without their energy being masked by the most energetic structures that dominate the flow far downstream and tend to mask the upstream organization when viewed using global SPOD. To explore the PIV dataset, we reduce the state vector to $\mathbf{q} = [u_x]^T$ and consider a matrix \mathbf{W} that contains trapezoidal quadrature weights for the uniform PIV grid. The CSDs are computed using Welch’s periodogram method. For the PIV data, we used blocks of 128 samples and 50% overlap, resulting in a resolution of $\Delta St = 0.0126$. For the LES data, larger blocks of 512 samples were used to achieve a resolution of $\Delta St = 0.0217$.

In the following, we show modal energy maps of the leading SPOD mode, which we associate with linear instability mechanisms, and infer changes in such mechanisms in the presence of the flight stream. This association is justified in regions of the spectrum where a large separation exists between its modal energy, $\lambda_1(m, St)$, and that of the first suboptimal mode, $\lambda_2(m, St)$ (even if a precise threshold for low-rank behavior is unclear). However, we stress that such comparisons should be made with care whenever the leading and suboptimal modes have comparable amplitudes. We emphasize that, in the following, the distinction between mechanisms concerns the flow response, given by SPOD and resolvent response modes, because the optimal forcing (in the framework of resolvent analysis) associated with KH and Orr structures display similar structures. It has been shown that KH wavepackets are also optimally forced by Orr-like structures on the vicinity of the nozzle [25,29,30]. Orr structures in the response, however, are characterized by lower phase speeds and extended spatial structure with respect to KH wavepackets. Figure 9 shows modal energy maps of the leading SPOD modes, $\lambda_{1_{m,\omega}}$ at the four streamwise positions considered previously. Superposed on these maps are contours of the ratio between the leading and first suboptimal eigenvalues, $\lambda_{1_{St,m}}/\lambda_{2_{St,m}}$. In both flow conditions, the energy peak occurs in the $St \rightarrow 0$ limit for azimuthal wave numbers $m > 0$. Following the downstream development of the jet, the wave number associated with the energy peak decreases monotonically, as already revealed in Figs. 7 and 8, but with the maximum energy always remaining in the $St \rightarrow 0$ zone. Downstream of the end of the potential core, mode $m = 1$ eventually becomes dominant, as observed previously in static jet conditions [31,32,60]. The flight stream is seen to produce a significant reduction of the energy levels, attenuating the first 15–20 azimuthal wave numbers. Closer to the nozzle exit, this reduction is seen to take place for a broad range of Strouhal numbers and azimuthal wave numbers. As the jet evolves downstream, the attenuation gradually becomes concentrated around the energy peak, which occurs at low St . This reveals that much of the reduction in turbulent kinetic energy observed in many previous studies, and described as a global attenuation of turbulence, is in fact underpinned by low-frequency, streaklike structures.

Besides the energy attenuations, the flight stream also produces a significant effect on the eigenvalue separation. Close to the nozzle exit, $\lambda_{1_{St,m}}/\lambda_{2_{St,m}}$ is reduced for almost all the azimuthal wave numbers in the range $St \gtrsim 0.2$. As the jet evolves downstream, this decrease in eigenvalue separation gets gradually concentrated at lower St and lower m , following the shift in energy peak. This implies that the energy attenuation is accompanied by a weakening of the leading SPOD modes which describe the most energetic, coherent flow structures. These have been shown to be associated with modal and nonmodal linear instability mechanisms [31,32]. In the initial jet region, modal growth mechanisms are strong, with KH wavepackets being convectively unstable for a broad range of frequencies starting from $St \gtrsim 0.1$ and azimuthal wave numbers $m < 5$, as will be shown shortly by the linear mean-flow analysis. Nonmodal mechanisms, which dominate the energy spectrum throughout the jet, give rise to Orr ($m = 0$) and streaky, lift-up ($m > 0$) structures, and have peak energy in the $St \rightarrow 0$ limit. The modal maps shown here suggest an attenuation of these three mechanisms, as revealed by both the energy reduction and the lower eigenvalue separation, which will be confirmed shortly following a comparison with a linear mean-flow model. Apart from the

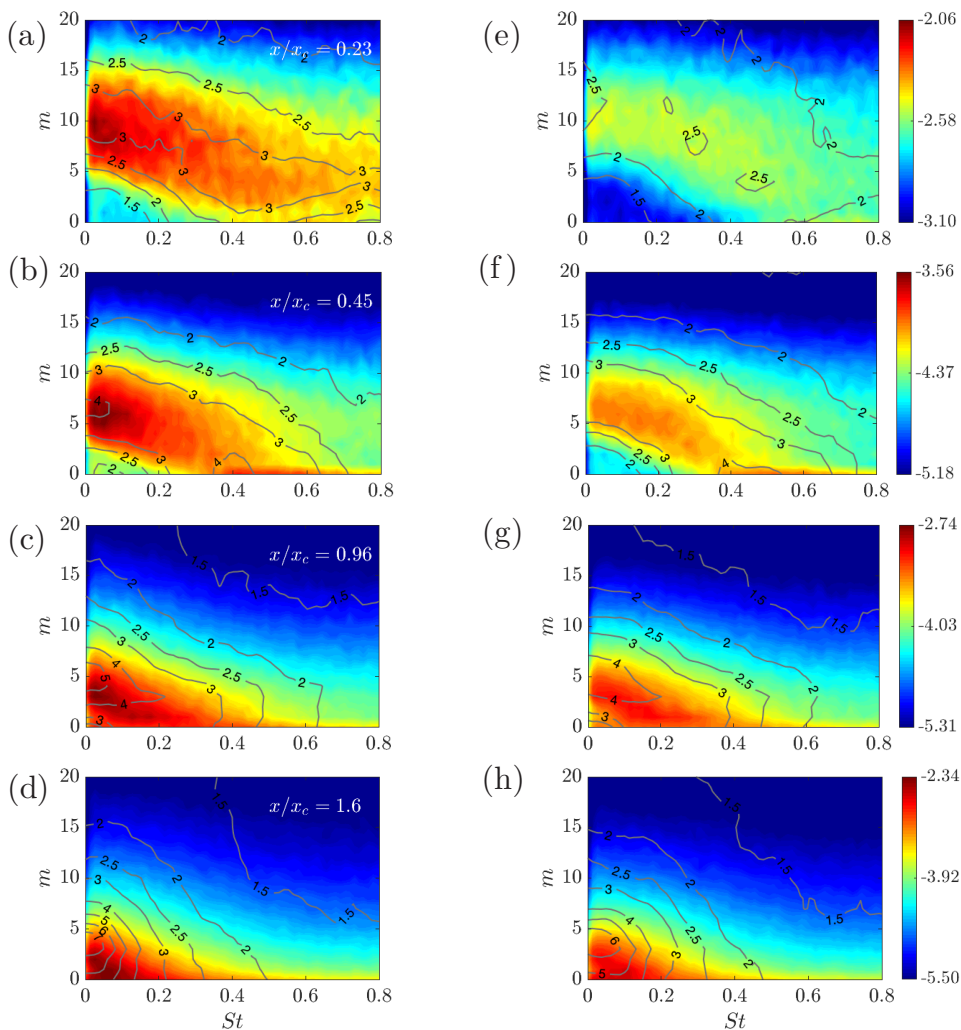


FIG. 9. Modal energy maps obtained through SPOD of PIV data. (a)–(d): maps for the $M_f = 0$ case; (e)–(h): maps for the $M_f = 0.15$ case. Colormaps correspond to the leading eigenvalue, $\log_{10}(\lambda_{1St,m})$. Gray contours represent values of the ratio between the leading and first suboptimal eigenvalues, $\lambda_{1St,m}/\lambda_{2St,m}$.

overall reduction in levels, it is also interesting to assess whether the flight stream changes the energy distribution in the St - m plane. Figure 10 shows modal energy maps normalized by their maxima. The normalization reveals that, for a given m , the spectrum is much broader in the St direction with the flight stream, especially upstream of the end of the potential core. Whereas in the $M_f = 0$ case the peak in the spectrum is concentrated in the $St \rightarrow 0$ region, for the $M_f = 0.15$ case it flattens and spreads to higher St . This shows that the effect of the flight stream is not limited to a simple rescaling of turbulence levels due to the reduced shear. In Sec. VII, we interpret the broadening of the spectrum in light of stability characteristics of the flow. Interestingly, the azimuthal organization of the energy is less affected by the flight stream. This can be illustrated by the different normalization of modal energy shown in Appendix A, and also by the scaling introduced in Figs. 7 and 8.

The results presented in Sec. IV–VI provide a comprehensive view of the effect of the flight stream, starting from zeroth order statistics, down to a more detailed analysis, through successive

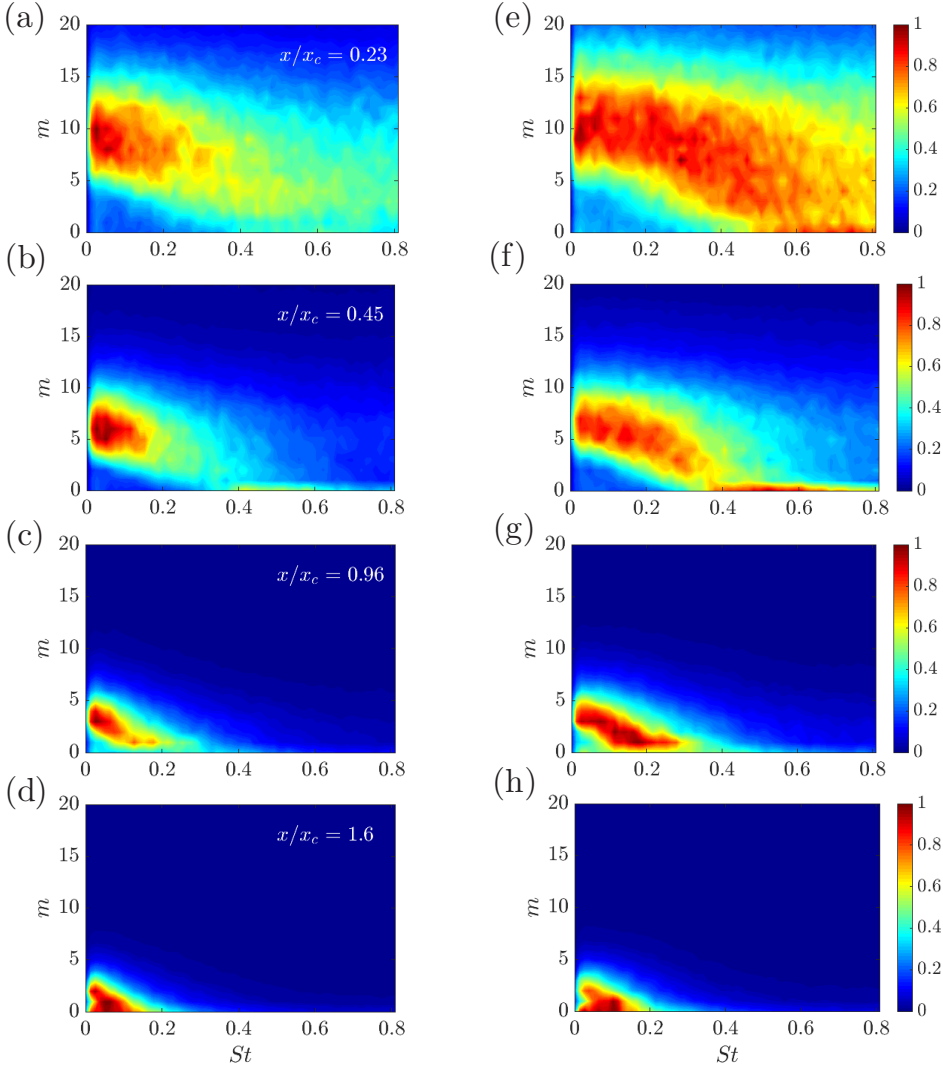


FIG. 10. Normalized modal energy maps of the leading SPOD mode, $[\lambda_{1st,m}/\max(\lambda_{1st,m})]$ in the frequency-azimuthal wave-number space for different streamwise positions based on PIV data. (a)–(d) Maps for the $M_f = 0$ case; (e)–(h) maps for the $M_f = 0.15$ case.

Fourier and modal decompositions, of how these changes are arranged in the frequency-wave-number space, and how they vary in the streamwise direction. Comparisons between the streamwise evolution of jets with and without the flight stream on the basis of the normalized coordinate, x/x_c , produce an interesting similarity in certain properties of the flow between the flight and static cases. The centerline velocity profiles for different flight-stream velocities collapse when the normalization is applied. The azimuthal organization of energy for the two jets are found to be in good agreement for equal x/x_c . The shape of the spectra are quite similar, as shown in Figs. 7 and 24. Furthermore, the most energetic azimuthal modes, $m_{\max}(x/x_c)$ are also very similar, decaying exponentially with increasing x/x_c at a rate which is virtually the same in the flight and static cases. Discrepancies are, however, manifest in the near-nozzle region, where the azimuthal spectra for the flight case are flatter and the peak is shifted toward higher m . Interestingly, it is in the same region that the eigenvalue

separation, $\lambda_{1_{St,m}}/\lambda_{2_{St,m}}$ is significantly reduced by the flight stream. This indicates a reorganization of the flow in which fluctuation energy is underpinned by somewhat more “disorderly” motion at higher m at the expense of the most coherent structures associated with the leading SPOD mode.

Other flow properties scale less well with x_c . For instance, collapse of the momentum thickness as a function of x/x_c is not observed. Normalized modal maps [$\lambda_{1_{St,m}}/\max(\lambda_{1_{St,m}})$] for the two jets are also found to be quite different, with the flight-stream-producing spectra which are broader in the St direction at a given x/x_c . This behavior is more pronounced in the initial jet region. As will be explained in the next section, these two trends are connected. The slower growth of the shear layer leads to a broader range of unstable frequencies, which can be associated with the broader spectrum.

VII. LINEAR MEAN-FLOW ANALYSIS

The results reported above raise the question as to what causes the observed energy attenuation. Is it simply a mean-flow modification effect (and in this case it is something that can be mimicked through a linear model), or is it rather due to a deeper (nonlinear) reorganization of turbulence? We address this issue through a locally parallel linear model, where linearization is performed about the mean flow. As discussed in section Sec. I, although in a laminar regime, with instability analysis performed about a fixed point, the reduction of shear produced by the flight stream is expected to attenuate modal and nonmodal instabilities by linear mechanisms alone, this scenario cannot be accepted, *a priori*, for the case of a turbulent jet. In the latter case nonlinearities, other than those that underpin the mean flow, may play an important role in the changes observed in the energy spectrum. It is therefore important to assess to what degree linear mean-flow mechanisms are the cause of the different dynamics observed with the flight stream in this high-Reynolds-number, turbulent regime.

The analysis starts with the linearized Navier-Stokes equations written in an input-output form:

$$\frac{\partial \mathbf{q}'}{\partial t} + \mathcal{A}_{\bar{\mathbf{q}}} \mathbf{q}' = \mathbf{f}, \quad (5)$$

where \mathbf{q}' is a vector containing fluctuations (in a Reynolds-decomposition sense) of the state variables and $\mathcal{A}_{\bar{\mathbf{q}}}$ is the linearized Navier-Stokes operator. The subscript $\bar{\mathbf{q}}$ denotes linearization about the mean flow. \mathbf{f} is a term representing the nonlinear Reynolds stresses, which are treated as an endogenous forcing term. In the locally parallel framework, we assume flow perturbations of the form

$$\mathbf{q}'(x, r, \theta, t) = \hat{\mathbf{q}}(r) \exp^{i(\alpha x - \omega t + m\theta)}, \quad (6)$$

where the radial structure of the perturbations is given by $\hat{\mathbf{q}}(r)$, α and m are streamwise and azimuthal wave numbers, respectively, and ω is the frequency. Applying a Fourier transform in Eq. (5) and substituting the *Ansatz* in Eq. (6) yields

$$-i\omega \hat{\mathbf{q}} + (\mathcal{A}_0 + \alpha \mathcal{A}_1 + \alpha^2 \mathcal{A}_2)_{\bar{\mathbf{q}}} \hat{\mathbf{q}} = \hat{\mathbf{f}}, \quad (7)$$

where the linear operators \mathcal{A}_0 , \mathcal{A}_1 , and \mathcal{A}_2 contain terms issuing from zeroth, first and second order derivatives in x , respectively. The superscripts $\hat{\cdot}$ denote Fourier transformed quantities. Details about the linearization procedure, the operators and the boundary conditions are given in Appendix B.

We carried out the analysis in the initial jet region. The mean flow profiles that served as input to the model were based on experimental data, and fitted with the hyperbolic tangent profiles proposed by Michalke *et al.* [35]. At frequencies for which the flow experiences a strong modal convective instability, it is known that eigenanalysis based on a spatial stability formulation provides a suitable framework to describe coherent structures in jets [33]. When the modal instability is weak other approaches should be used to study linear mechanisms. We address such cases with a model based on the response modes of the resolvent operator. Since the work of McKeon and Sharma [62],

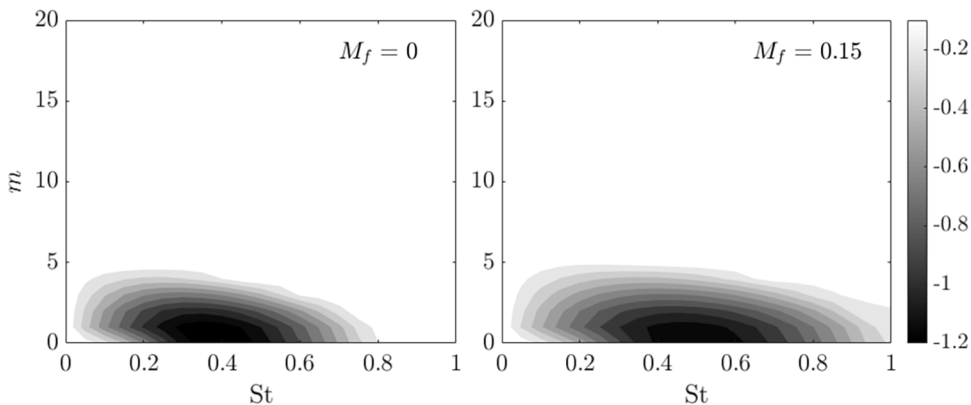


FIG. 11. Contours of the growth rates, α_i , of the Kelvin-Helmholtz mode in the St - m plane, computed at $x/x_c = 0.23$.

resolvent analysis has been extensively used to identify optimal forcing and response mechanisms in laminar and turbulent flows and to model observed coherent structures.

A. Eigenanalysis: Spatial stability

In eigenanalysis, the nonlinear forcing terms are assumed negligible. The linearized Navier-Stokes system can then be recast in the form of an eigenvalue problem. We here consider the spatial stability problem, for which the eigenvalue problem is given by

$$\mathbf{L}\hat{\mathbf{q}} = \alpha\mathbf{F}\hat{\mathbf{q}}, \quad (8)$$

where $L = -\omega\mathbf{I} + \mathcal{A}_0$ and $F = -\mathcal{A}_1$. For high Reynolds numbers such as those considered here, Rodríguez *et al.* [63] have shown that α^2 viscous terms can be neglected. The streamwise evolution of disturbances is governed by the sign of the imaginary part of the wave number, α_i . If $\alpha_i < 0$, then disturbances grow exponentially in the positive x direction. In the following, we analyze the behavior of the most unstable mode given by Eq. (8), which corresponds to the Kelvin-Helmholtz instability. Figure 11 shows contours of α_i in the St - m plane for instability analyses performed at $x/x_c = 0.23$. A region of strong convective instability is seen for $m = 0$ – 4 on a broad range of Strouhal numbers. Higher azimuthal wave numbers were found to be stable for all Strouhal numbers analyzed. As the jet evolves downstream, the region of convective instability gradually shifts to lower frequencies (not shown), following the thickening of the shear layer. This is followed by a reduction of growth rates and eventual stabilization of the Kelvin-Helmholtz mode, as will be shown shortly; therefore, the $St \rightarrow 0$ region is always characterized by low growth rates. We note two important changes in the instability contours with the flight effect: a shift of the peak α_i to higher St and a broader range of unstable frequencies. These changes are associated with the fact that the shear-layer thickness evolves at different rates for the two jets. As shown in Fig. 5, normalizing the streamwise coordinate by x_c corrects some of the discrepancy but does not eliminate it entirely, and the shear layer in the $M_f = 0$ still grows at a faster rate; therefore, for the same x/x_c , the jet with the flight stream has a smaller δ_θ . The thinner shear layer causes the most amplified mode to occur at a higher frequency, and the range of unstable frequencies to be broader. The broader range of amplified disturbances in turn offers more possibilities for nonlinear interactions between those disturbances to occur. This may explain why the flight stream produces a broader spectrum in the near-nozzle region, as seen in Fig. 10.

These changes are followed by a decrease in the peak growth rates, as can be more clearly seen in Fig. 12 for the $m = 0$ and $m = 1$ azimuthal modes. To correct the discrepancy, Michalke and Hermann [35] proposed a scaling of the growth rates and frequencies by a “stretching factor,” derived

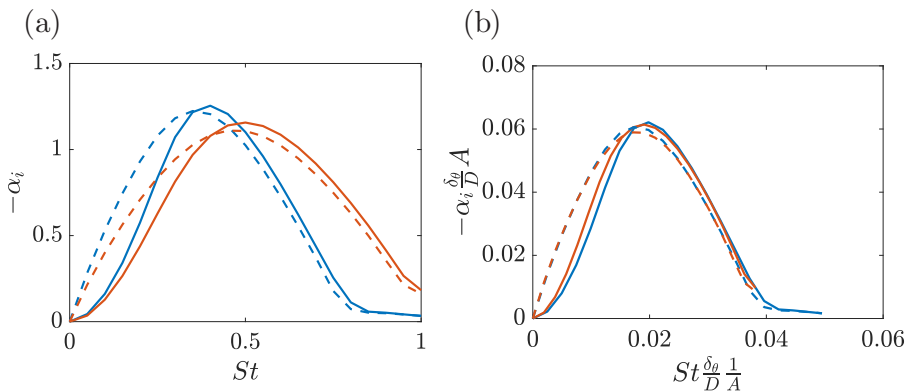


FIG. 12. Growth rates of the Kelvin-Helmholtz instability for azimuthal modes $m = 0$ and $m = 1$ at $x/x_c = 0.23$. In panel (a), as a function of Strouhal number. In panel (b), the Strouhal number and growth rates are normalized using the local momentum thickness, δ_θ/D , and a stretching factor, A , which we define as the ratio between the potential core lengths in the flight and static cases. —: $m = 0, M_f = 0$; - - -: $m = 1, M_f = 0$; —: $m = 0, M_f = 0.15$; - - -: $m = 1, M_f = 0.15$.

from similarity considerations, $A = 1 + \Delta U/c_n U_f$, where $\Delta U = U_j - U_f$ and c_n is a neutral phase velocity (we have adapted their variable nomenclature to avoid confusion with ours). This scaling was found to provide a reasonable match for the modified growth rates, $\alpha_i \delta_\theta / D$ and frequencies, $\omega \delta_\theta / (\Delta U A)$ for jets in static and flight conditions. However, the stretching factor is not universal, but a function of m and δ_θ . Furthermore, the match worsens with increasing shear-layer thickness, due to deviations from the hypotheses made in the derivation. Here we propose a scaling with a fixed stretching factor, given simply by the ratio between potential core lengths, $A = (x_c)_f / (x_c)_s$, where the subscripts f and s refer to the static and flight cases, respectively. The modified growth rates and Strouhal numbers are thus given as $-\alpha_i \delta_\theta / D A$ and $St \frac{\delta_\theta}{D} \frac{1}{A}$. Figure 12(b) shows that the scaled curves are in excellent agreement, both in the frequency of the peak and its magnitude. Similar agreements were found for other x/x_c in the initial jet region. Figure 13 shows the streamwise evolution of the Strouhal number of the most amplified mode for the $m = 0$ wave number. When corrected by the stretching parameters, the peak Strouhal numbers, $St_{\max} \frac{\delta_\theta}{D} \frac{1}{A}$, are found to be virtually the same for

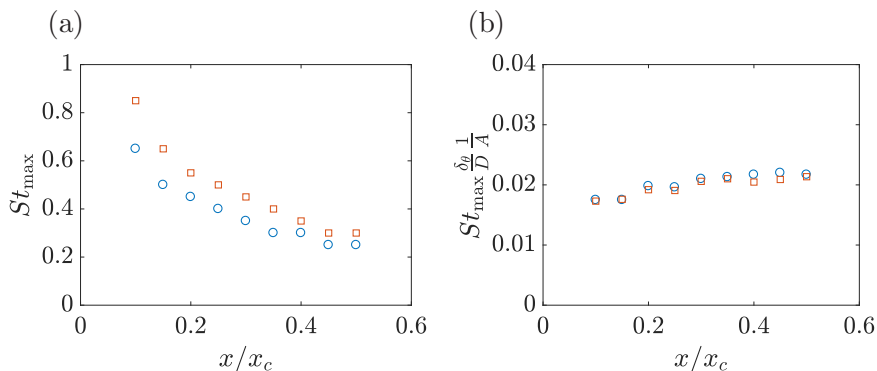


FIG. 13. (a) Strouhal number corresponding to the peak growth rate for the $m = 0$ azimuthal wave number at different streamwise positions. In panel (b), the values are scaled by the local momentum thickness and the stretching factor, A , and a match is obtained for the flight and no-flight cases. Circles and squares correspond to the $M_f = 0$ and $M_f = 0.15$ cases, respectively.

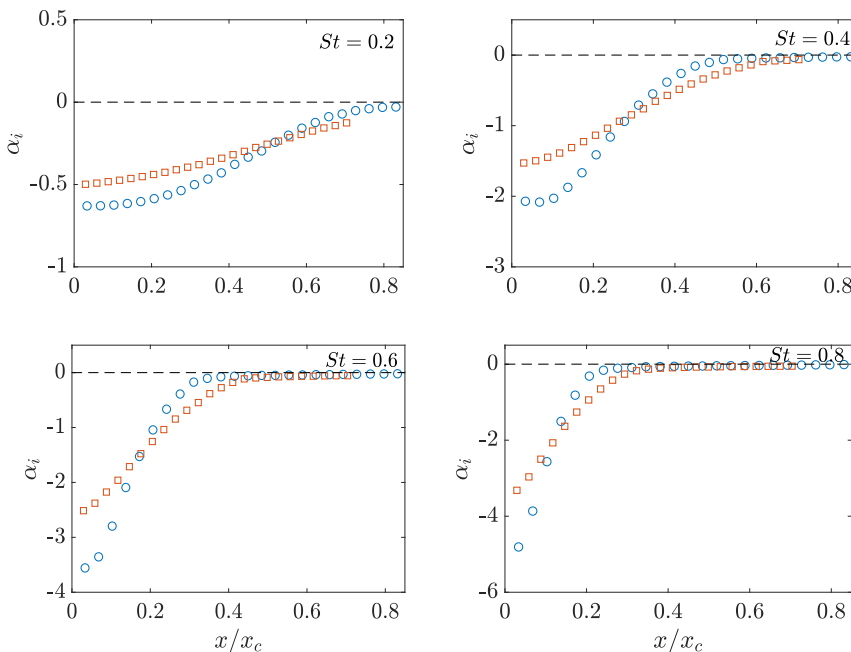


FIG. 14. Streamwise evolution of the growth rates of $m = 0$ KH wavepackets for $St = 0.2, 0.4, 0.6, 0.8$. Circles and squares correspond to the $M_f = 0$ and $M_f = 0.15$ cases, respectively. The black-dashed line corresponds to the $\alpha_i = 0$, limit, when the KH mode becomes stable.

two jets, and to be nearly independent of streamwise position. This scaling shows therefore that the frequency shift of the most unstable wave number is related to the shift in the potential core length.

Figure 14 shows the streamwise evolution of the axisymmetric KH growth rates for four Strouhal numbers within the unstable range. For a given St , growth rates in the flight case are lower close to the nozzle exit. However, without the scaling, they decay at a slower rate, due to the slower growth of the momentum thickness, and the stabilization predicted by the model occurs further downstream than in the static case. The changes in growth rates are followed by an increase in phase velocity, as shown in Fig. 15 for the $m = 0$ mode. Other azimuthal wave numbers (not shown) display the same behavior. Figure 15 also shows that, in Strouhal numbers for which the KH instability is stronger ($St = 0.4\text{--}0.6$ at $x/x_c = 0.23$), scaling the phase velocities of the flight-stream case with A makes them collapse with those of the static case.

The stabilization of the Kelvin-Helmholtz mechanism with the flight stream is consistent with the energy reduction at low m seen in the modal energy maps depicted in Fig. 9 in the range $0.4 \leq St \leq 0.8$. It also explains the reduction in the $\lambda_{1St,m}/\lambda_{2St,m}$ ratio seen in the near-nozzle region. Previous studies showed the leading SPOD mode to be underpinned by the KH mechanism in this region [14,29,30,32]. A less unstable KH mechanism then leads to a less dominant leading SPOD mode, and therefore a smaller separation with respect to suboptimal modes.

B. $St \rightarrow 0$ limit: Resolvent analysis

As seen in Fig. 11, at low St the growth rates are small, and therefore the KH modal instability mechanism is weak. Nonmodal mechanisms, such as the Orr and lift-up mechanism then become dominant, but the spatial stability framework is not suitable to describe them. Therefore, to model the linear mechanisms in that zone we use a local model based on the resolvent operator.

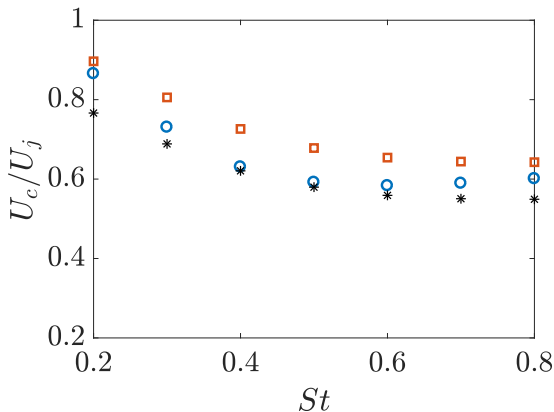


FIG. 15. Phase velocities of the $m = 0$ KH instability as a function of St computed at $x/x_c = 0.23$. Circles: $M_f = 0$; squares: $M_f = 0.15$. The asterisks represent the phase velocities of the flight case scaled by the A factor.

Equation (7) can be rewritten as

$$\hat{\mathbf{q}}_{\alpha,\omega,m} = \mathcal{C}(i\omega - \mathcal{A}_0 - \alpha\mathcal{A}_1 - \alpha^2\mathcal{A}_2)^{-1}\mathcal{B}\hat{\mathbf{f}}_{\alpha,\omega,m}, \quad (9)$$

where matrices \mathcal{B} and \mathcal{C} can be used to restrict forcing and response to a desired subspace [28]. In a more compact form, we can write

$$\hat{\mathbf{q}}_{\alpha,\omega,m} = \mathcal{R}_{\hat{\mathbf{q}},\alpha,\omega,m}\hat{\mathbf{f}}_{\alpha,\omega,m}, \quad (10)$$

where $\mathcal{C}(i\omega - \mathcal{A}_0 - \alpha\mathcal{A}_1 - \alpha^2\mathcal{A}_2)^{-1}\mathcal{B}$ is the resolvent operator. For both the spatial stability problem and resolvent analysis discretization in the radial direction is carried out using Chebyshev collocation points. The domain is extended to the far-field by mapping the original domain, $r \in [-1, 1]$ to $r \in [0, \infty)$ using the function proposed by Lesshafft *et al.* [64] and concentrating most points in the potential core and shear layer. The goal of resolvent analysis is to seek an optimal forcing that maximizes the norm of the associated flow response,

$$\sigma^2 = \max_{\hat{\mathbf{f}}_{\alpha,\omega,m}} \frac{\|\mathcal{R}_{\hat{\mathbf{q}},\alpha,\omega,m}\hat{\mathbf{f}}_{\alpha,\omega,m}\|_{\mathbf{W}_q}^2}{\|\hat{\mathbf{f}}_{\alpha,\omega,m}\|_{\mathbf{W}_f}^2}, \quad (11)$$

where \mathbf{W}_q and \mathbf{W}_f are positive definite Hermitian matrices representing the weights of the norms of response and forcing, respectively. The maximization of the forcing can be achieved through a singular-value decomposition (SVD) of the resolvent operator,

$$\mathbf{W}_q^{-1/2}\mathcal{R}_{\hat{\mathbf{q}},\alpha,\omega,m}(\mathbf{W}_f^{-1/2})^H = \mathbf{U}\mathbf{\Sigma}\mathbf{V}^H, \quad (12)$$

where the superscript H denotes Hermitian transpose and $\mathbf{W}_{f,q}^{-1/2}$ are defined by a Cholesky decomposition. Forcing (\mathbf{u}_i) and response (\mathbf{v}_i) modes are defined as $\mathbf{v}_i = (\mathbf{W}^{-1/2})^H\mathbf{V}_i$ and $\mathbf{u}_i = (\mathbf{W}^{-1/2})^H\mathbf{U}_i$, with i denoting the i th column of \mathbf{V} and \mathbf{U} . The singular values associated with each forcing-response pair, σ_i , are arranged in descending order in the diagonal matrix $\mathbf{\Sigma}$.

Following Nogueira *et al.* [31,65,66], we apply the following weighting function to the response,

$$\mathbf{W}_q = \text{diag}[0.5(1-b)(1 + \tanh(r_p/D) - r/D) + b]\mathbf{W}_{\text{cheb}}, \quad (13)$$

which is designed so as to localise responses inside the region of high shear and avoid the appearance of free-stream modes, mitigating the dependence of the results on domain size [66]. \mathbf{W}_{cheb} are the quadrature weights for the Chebyshev grid. The value of $r_p/D = 1$ is chosen so that the weights

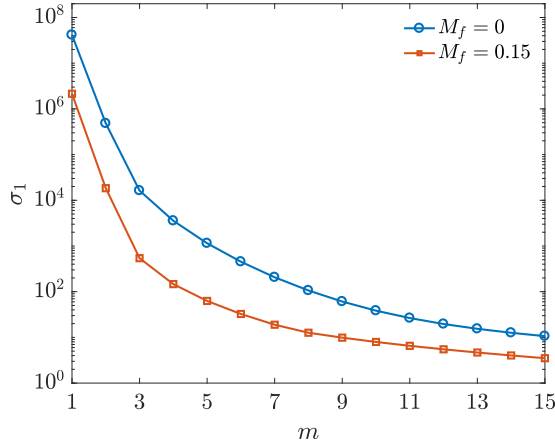


FIG. 16. Optimal resolvent gains, σ_1 , as a function of azimuthal wave number, m , computed for $\omega = 0$ and $\alpha = 0$.

are zero far from the sheared region. b is a small positive parameter used to avoid zero weights at large r/D . No spatial restriction is applied to the forcing weight, so that $\mathbf{W}_f = \mathbf{W}_{\text{cheb}}$. With this choice of parameters, we seek an optimal forcing whose associated response is maximized inside the jet core and shear layer, $r/D \lesssim 1$. The locally parallel resolvent analysis is carried out at a fixed streamwise position using the mean flow, α , ω , and m as inputs.

For high-Reynolds-number flows such as the one considered here, recent studies have explored the use of eddy-viscosity models as a means to improve agreement between the model and coherent structures observed in flow data [29,67–74]. The eddy-viscosity provides a partial inclusion of nonlinear effects in the linear operator, beyond the simple establishment of the mean-flow, and good agreement may be obtained in both cases with an effective Reynolds number that is substantially lower than the molecular one. Here we consider a radially constant eddy-viscosity, following the approach of Kuhn *et al.* [74]. It is known that constant eddy-viscosity fields do not capture the intermittent boundary of the flow, where fluctuations change from rotational to potential. We do not expect the model to capture intermittency effects. However, it was shown by Kuhn *et al.* [74] that the use of radially dependent eddy-viscosity only improves marginally the results of local mean-flow models. The magnitude of ν_T is determined from a least-square fit of the $\overline{u'_x u'_r}$ component of Reynolds tensor based on a Boussinesq model,

$$\tilde{\nu}_T = -\frac{\overline{u'_x u'_r}}{d\overline{U}/dr}, \quad (14)$$

with $\tilde{\nu}_T = \nu_T/(U_j D)$ being a nondimensional kinematic viscosity. Considering mean velocity and Reynolds tensor profiles at $x/x_c = 0.23$, data for the $M_f = 0$ case yields $\tilde{\nu}_T = 0.0017$, which corresponds to a turbulent Reynolds number of $\text{Re}_T = \tilde{\nu}_T^{-1} = 588$. For the sake of simplicity, we keep this value of Re_T for the static and flight cases.

In the following we show results of resolvent analyses performed in the initial jet region. We consider a range of parameters at which the flow is expected to be dominated by streaky structures generated by the lift-up effect. These structures exist for nonzero azimuthal wave numbers and are characterized by slow timescales and low streamwise wave numbers. We therefore set $\omega = 0$, $\alpha = 0$, and $m > 0$. Inspection of the energy maps in Figs. 9(b) and 9(f) show that, in the $\text{St} \rightarrow 0$ limit, the first ten to fifteen azimuthal wave numbers observed in the experiment are weakened by the flight stream. This trend was found to be correctly captured by the resolvent model. Figure 16 displays the leading resolvent gains as a function of m computed with mean velocity profiles measured at $x/x_c = 0.23$. The leading gain is reduced for all m with the flight stream.

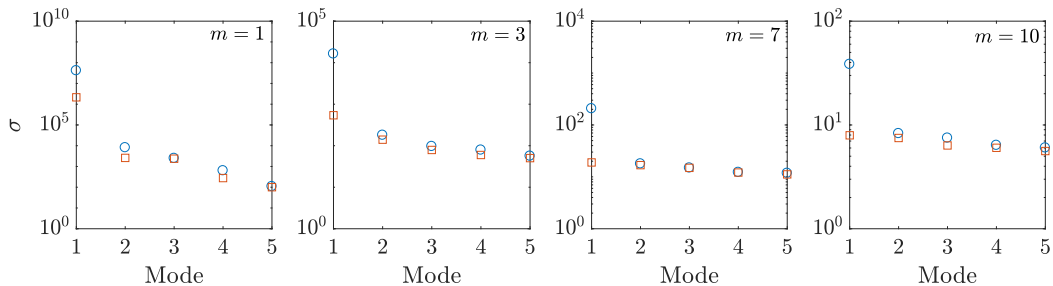


FIG. 17. Optimal and first four suboptimal resolvent gains, σ_{1-5} computed for $\omega = 0$ and $\alpha = 0$. Circles: $M_f = 0$; squares: $M_f = 0.15$.

The model does not predict correctly the azimuthal wave number of the peak energy. It is seen in Figs. 9(b) and 9(f) that the peak energy occurs at $m = 5$, whereas the model predicts gains that decay monotonically for $m \geq 1$. This is a limitation of the local model, which predicts the gain and shape of optimally forced structures that, from a given streamwise position, will grow downstream as they are convected with the parallel mean flow. The highest gain computed for the model is for $m = 1$. Indeed, further downstream the $m = 1$ mode does become dominant; but because the local model does not take into account the upstream amplification of higher wave numbers, it is not equipped to provide the correct shape of the energy spectrum at that position. For this reason, we limit our discussion of the resolvent analysis to global differences in gain between the $M_f = 0$ and $M_f = 0.15$ cases. In that sense, the reduction in gains agrees with the trends of the energy maps based on the data, showing that the attenuation observed in the experiment may be associated with the attenuation of linear (mean-flow) growth mechanisms.

Figure 17 shows a comparison between the leading gain and the first four suboptimal gains for selected m . It can be seen that, contrary to σ_1 , the suboptimal gains are not strongly affected by the flight stream, and therefore the separation between σ_1 and σ_2 is significantly reduced. This suggests that the attenuation of the associated flow structures is produced mainly by a weakening of the optimal mechanism. This is consistent with results of the SPOD analysis, which showed a reduction of the modal energy separation, λ_1/λ_2 , in the flight-stream case, and suggests that the rank-reduction in the initial jet region is produced by a linear mechanism. This trend was also verified using other values of Re_T .

Figure 18 shows SPOD and optimal resolvent response modes computed at $m = 6$. The modes are reconstructed in the y - z plane using the Ansatz $\Psi_1, \mathbf{u}_1 = \hat{u}_x(r)e^{im\theta}$, where $\hat{u}_x(r)$ is the radial structure issuing from the SPOD and resolvent calculations. The streaky structures possess no support in the jet core, and are confined to the shear layer. Due to the thinner shear layers, in the flight-stream case the streaks become more radially compact and their peak shifts to a smaller r/D . These trends are well captured by the resolvent model. The resolvent modes display a slower decay in r/D with respect to the SPOD, which is something that had also been observed by Nogueira *et al.* [31].

Overall, the linear mean flow models are able to mimic two important trends seen in the energy maps of experimental data: the stabilization of the KH and lift-up mechanisms and a weakening of the low-rank behavior of the jet on in extended regions of the St - m spectrum.

VIII. GLOBAL SPOD

We now move from the local framework of PIV data to a global SPOD analysis performed with the LES database. Our goal is to compare modal energy maps and to quantify the distortion of global SPOD modes by the flight stream. We consider the complete state variable vector, $\mathbf{q} = [\rho, u_x, u_r, u_\theta, T]^T$ in the entire available flow domain, $0 \leq x/D \leq 30$, $0 \leq r/D \leq 6$. The computed

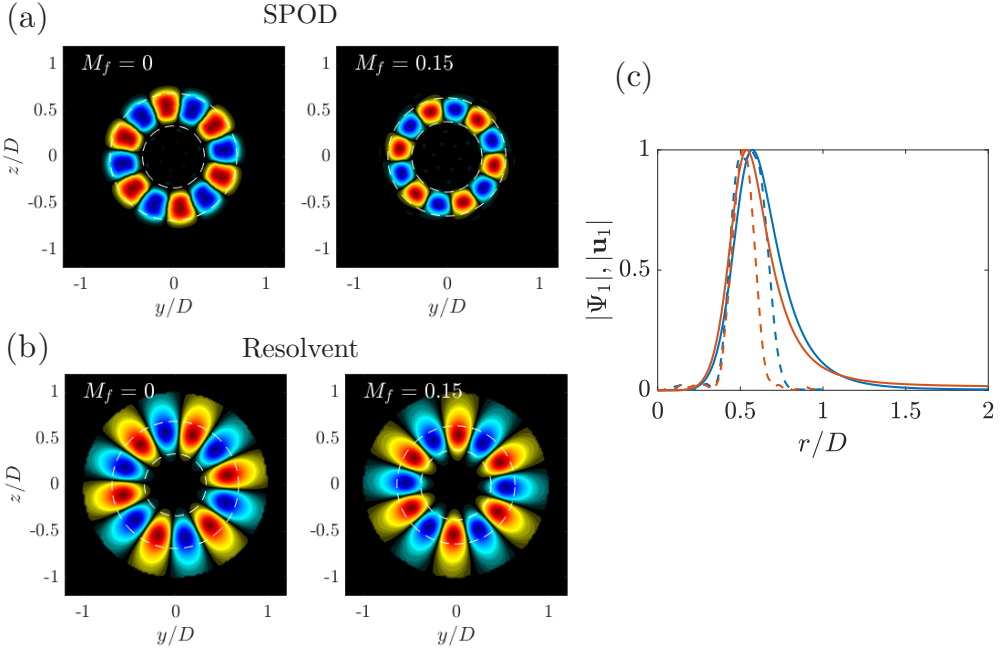


FIG. 18. Comparison between local streamwise velocity SPOD and resolvent response modes at $x/x_c = 0.23$ associated with $m = 6$ streaky structures. Panels (a) and (b) show reconstructions of the real parts of local modes in the y - z plane using the Ansatz $\Psi_1, \mathbf{u}_1 = \hat{u}_x(r)e^{im\theta}$. Contours are adjusted between 0 and 1. Panel (c) shows the absolute parts of the modes, $|\Psi_1|, |\mathbf{u}_1|$; —: leading resolvent mode for $M_f = 0$; —: leading resolvent mode for $M_f = 0.15$; - - -: leading SPOD mode for $M_f = 0$; - - -: leading SPOD mode for $M_f = 0.15$. The white dashed lines in panels (a) and (b) correspond to the positions where $\tilde{U}_x(x, r) = 0.99$ and $\tilde{U}_x(x, r) = 0.05$, roughly delimiting the shear layer.

modes are orthogonal with respect to Chu's energy norm [75]:

$$\langle \mathbf{q}_1, \mathbf{q}_2 \rangle_E = \iiint \mathbf{q}_1^* \text{diag} \left(\frac{\bar{T}}{\gamma \bar{\rho} M_j^2}, \bar{\rho}, \bar{\rho}, \bar{\rho}, \frac{\bar{\rho}}{\gamma(\gamma - 1)\bar{T}M_j^2} \right) \mathbf{q}_2 r dx dr d\theta. \quad (15)$$

Figure 19 shows eigenvalue spectra for the first five azimuthal wave numbers. Spectra for the axisymmetric mode display the known separation between the leading and first suboptimal mode for $St \gtrsim 0.3$ [29,30]. The low-rank behavior in that Strouhal number range becomes less and less marked with increasing wave number, a trend that was also observed by Schmidt *et al.* [29], and which is consistent with the weakening of the KH instability at higher m , as can be seen in Fig. 11. Spectra for the static and flight cases follow the same general trends; however, some important differences are observed in the eigenvalue separation.

Figure 20 shows contours of λ_1/λ_2 in the St - m plane. It can be seen that peak values of λ_1/λ_2 are reduced by the flight stream in the KH-dominated zone, which was also observed in the local SPOD maps. Moreover, the low-rank zone is broader and shifted toward higher St . These trends are consistent with the results of the local stability analysis, which predicted a larger range of unstable frequencies in the flight case, and a shift of the most unstable mode toward higher St . Interestingly, in the low St limit, the flight stream slightly increases the eigenvalue separation. This is contrary to what is observed in the PIV data up to $x/x_c = 1.6$, and suggests that further downstream the flight stream changes the dynamics of streaks in a non trivial manner. The precise mechanism by which this happens is not yet clear and is currently under investigation.

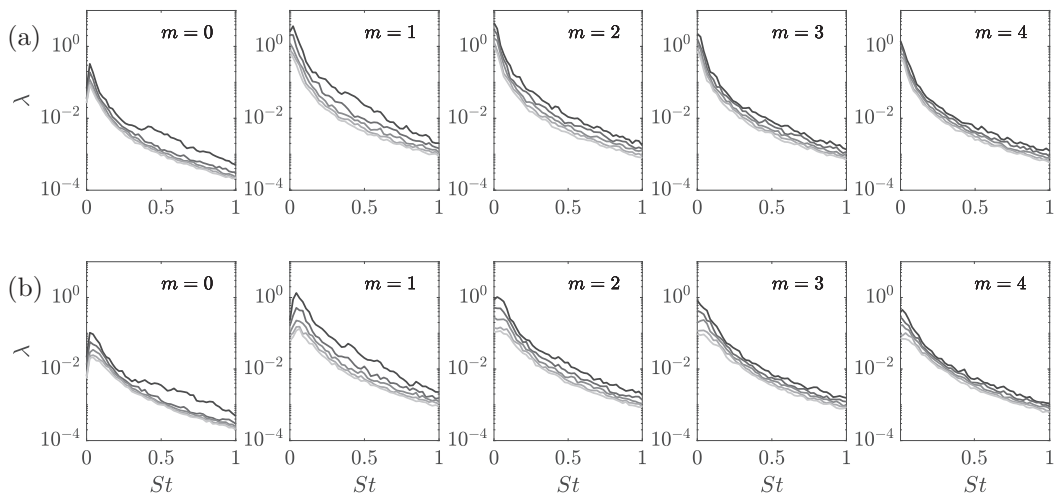


FIG. 19. Eigenvalue spectra of the global SPOD analysis modes performed with LES data. Color shading from black to white represent increasing mode numbers: (\blacksquare , $\lambda_1 > \lambda_2 > \dots > \lambda_5$); (a) $M_f = 0$; (b) $M_f = 0.15$.

The $St \rightarrow 0$ limit is also the region where the largest energy reductions occur, as clearly seen in the modal energy maps of the leading SPOD modes of Fig. 21. In the global framework, the modal energy spectrum is dominated, for a broad range of Strouhal numbers, by the $m = 1$ mode (the dominance of the $m = 1$ mode can also be observed in the results of Fig. 9 at downstream positions). In the zero-frequency limit, $St \rightarrow 0$, $m = 1-3$ modes are dominant. These trends are also found to hold in the presence of the flight stream. The attenuation of the $m = 1-3$ streaks, which are globally the most energetic structures of the flow, is the most striking modification. In Fig. 21(b), the modal maps are normalized by their respective maximum values. The normalization reveals a broader spectrum with the flight stream: while in the static case the peak is concentrated around $m = 2$ and $St \rightarrow 0$, in the flight case it spreads over $1 \leq m \leq 3$ and up to $St = 0.1$.

Figure 22 shows leading SPOD modes of streamwise velocity, $\Psi_1 : \hat{u}_x$, at different St and m representative of the Kelvin-Helmholtz, Orr, and lift-up mechanisms, according to the linear mechanism maps of Pickering *et al.* [32]. The KH-associated structures, here represented by the modes at $St = 0.6$, display the same characteristics described in previous studies [25,29,30]: organized

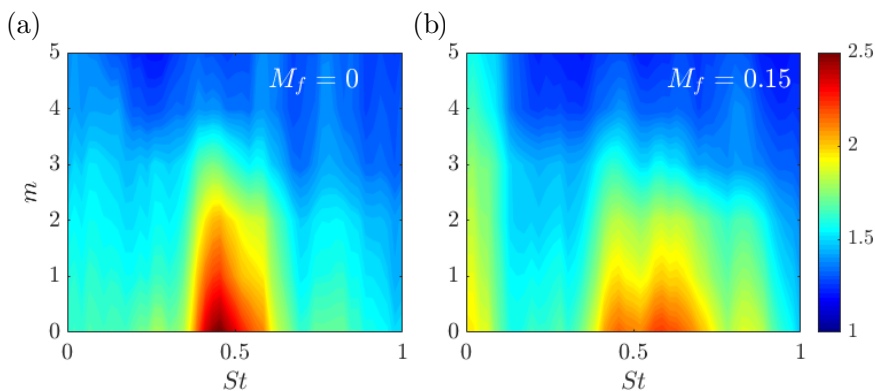


FIG. 20. Contours of the ratio between the leading and first suboptimal eigenvalues, $\lambda_{1St,m}/\lambda_{2St,m}$, from global SPOD for (a) the static case and (b) the flight case.

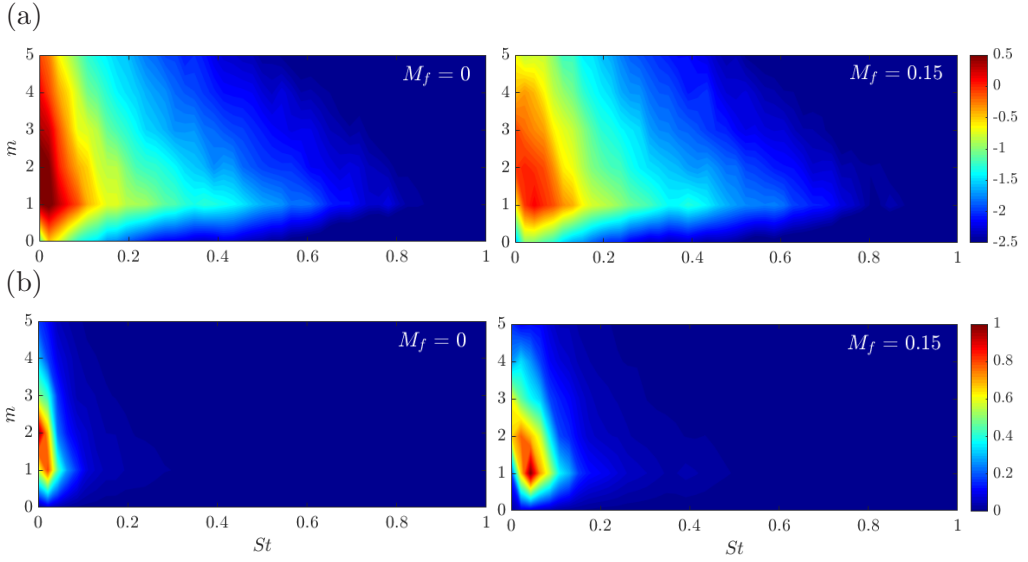


FIG. 21. Modal energy maps of the leading SPOD mode. In panel (a), contours of $\log_{10}(\lambda_{1St,m})$ are shown. In panel (b), the maps are normalized by their maximum $[\lambda_{1St,m} / \max(\lambda_{1St,m})]$.

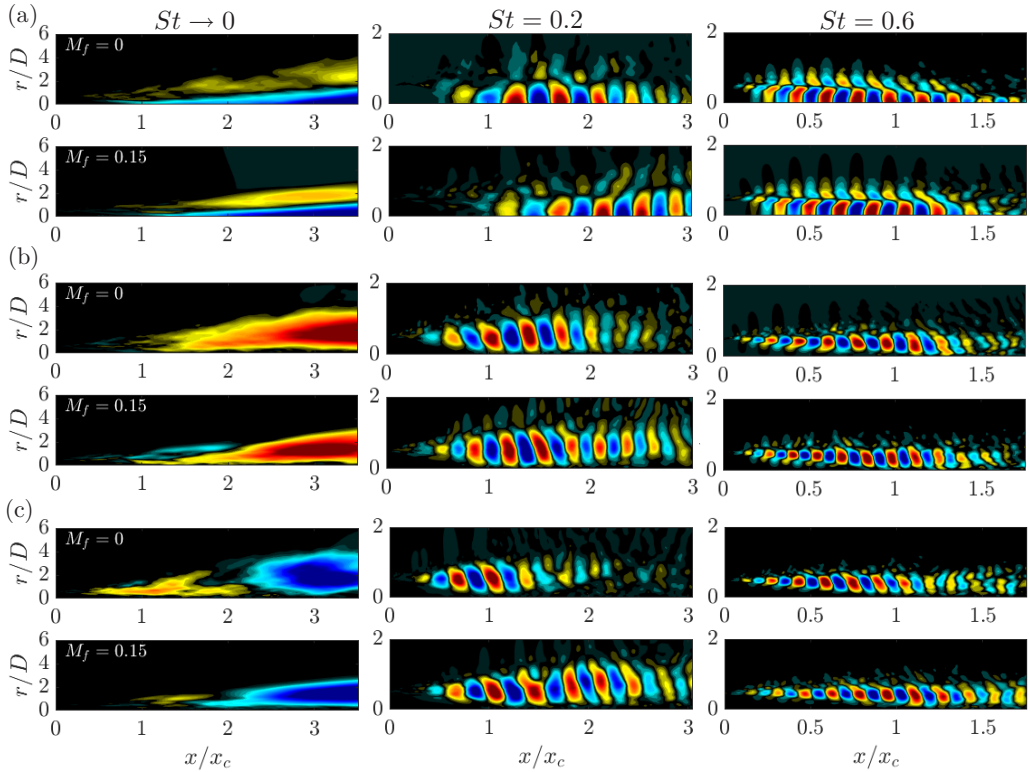


FIG. 22. Real part of global leading SPOD modes of streamwise velocity, $\text{Re}(\Psi_1 : \hat{u}_x)$, at Strouhal numbers and wave numbers representative of the lift-up, Orr, and Kelvin-Helmholtz instability mechanisms. Panels (a)–(c) are for azimuthal modes $m = 0, 2, 3$, respectively.

structures that grow in the first jet diameters, stabilize, and decay toward the end of the potential core. As the mode order is increased, the structure of the Kelvin-Helmholtz wavepackets is seen to lose their support in the jet core and to become confined to the shear layer. That applies to structures found in both jets. The flight stream does not lead to any substantial change in the underlying spatial structure of the KH instability. The reduction in growth rates predicted by the linear model are not manifest in Ψ , but rather in the modal energies. The linear model also predicts an increase in phase velocity with the flight stream, which in principle causes a change in the spatial wavelength of the modes; however, for Strouhal numbers around $St = 0.4$ – 0.6 , the change in phase velocity in the initial jet region was found to scale approximately with x_c , as shown in Fig. 15, so that when plotted as a function of x/x_c , the wavelengths of the leading SPOD modes look quite similar.

The structures associated with the Orr mechanism ($m = 0$, $St = 0, 0.2$) are more spatially extended and develop downstream of the end of the potential core [25,29,30]. In the zero-frequency limit, the most energetic structures correspond to streaks, which are characterized by very large wavelengths, and a slow spatial development, attaining their maximum far downstream. Here the effect of the flight stream is seen to be more marked: since streaks have spatial support in the jet shear layer, the thinner shear-layer thicknesses in the $M_f = 0.15$ case (see Figs. 3 and 5) produce streaks which are less extended in the radial direction. For small, but nonzero Strouhal numbers up to $St \approx 0.2$ and small, but nonzero wave numbers, the Orr mechanism is likely to be present, together with the lift-up mechanism [76–78]. This is reflected in the shapes of the SPOD modes at $St = 0.2$, $m = 3$, which bear some resemblance with the Orr structures found at $m = 0$, although they have less support in the jet core, as do the streaks at $St \rightarrow 0$.

The alignment between the SPOD modes computed in both flow conditions can be characterized in a quantitative manner through the following β metric,

$$\beta = |\Psi_1 \mathbf{W} \Psi_{1_f}|, \quad (16)$$

where the subscript f refers to the flight-stream case. Ψ_1 is the leading SPOD mode containing all flow variables. It represents a global alignment metric for the projection of the modes and varies from 0, if the modes are completely orthogonal, to 1, if they are perfectly aligned. The weight matrix \mathbf{W} accounts for the quadrature weights and Chu’s energy norm. In an attempt to see to what extent the potential core length collapses the overall flow organization, prior to computing β , the modes and mean flows are scaled by x_c . Furthermore, when computing the alignment at $St = 0.4, 0.6$, and 0.8 , the domain was restricted to $x/D = 15$, because downstream of those positions KH wavepackets lose much of their spatial support and the modes become noisy, thus biasing the alignment. Using the same reasoning, alignment for $St = 0.2$ was computed with a domain that extends up to $x/D = 25$. Figure 23 shows the values of β as a function of St and m . β assumes very high values for Strouhal numbers and wave numbers associated with KH wavepackets, confirming that their spatial shape is mostly controlled by the mean-flow stretching, and whose effect can be captured using the length of the potential core as a similarity. At Orr and lift-up dominated frequencies, the alignment between the modes is globally poorer than that of the KH mechanism, revealing that the associated flow structures are impacted in a more subtle way by the flight stream.

IX. CONCLUSIONS

In this work, we present high-fidelity experimental and numerical databases of subsonic turbulent jets subject to flight streams. 2D-PIV experiments were first performed aiming at quantifying the evolution of first-order velocity statistics with increasing flight-stream Mach numbers. The main effects of the flight stream on these were found to follow the trends reported in previous studies, namely: a stretching of the jet potential core, reduction of shear-layer thicknesses, and a reduction of turbulent intensities all over the jet domain. The main motivation of the present study is to perform an analysis of the energy distribution in a large region of frequency-wave-number space. Such analysis requires time-resolved data in the r - θ plane; for that, extensive cross-plane, stereoscopic,

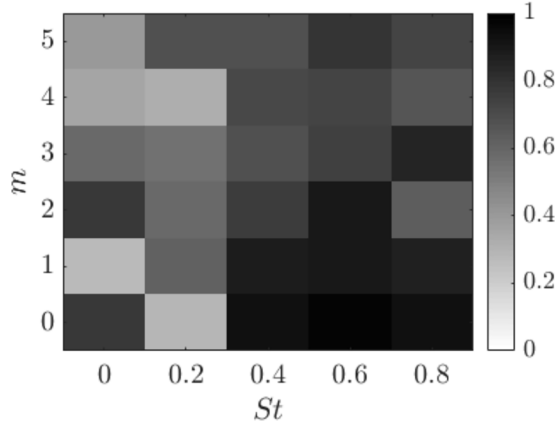


FIG. 23. β metric for the alignment of global leading SPOD modes, Ψ_1 , with and without the flight stream.

time-resolved PIV experiments were performed in a streamwise region ranging from the near-nozzle region to twice the potential core length, x_c . Two flow conditions were chosen for the analysis, $(M_j, M_f) = (0.9, 0)$ and $(M_j, M_f) = (0.9, 0.15)$. Companion LES simulations are also performed, and found to be in excellent agreement with the experimental data. The experimental and numerical databases are used to perform local and global SPOD, respectively, and to compute modal energy maps. Apart from the well-known attenuation of the modal KH instability mechanism [35,36], here we also report, to the best of our knowledge for the first time, striking energy reductions in regions of the frequency-wave-number space associated with the Orr and lift-up nonmodal mechanisms. The effect of the flight stream is found to be manifest in different aspects of coherent structure dynamics and energy organization that go beyond the simple attenuation of turbulent energy due to the reduced shear.

The attenuation of coherent structures occurs from the very near-nozzle region and is accompanied by a weakening of the low-rank dynamics of the jet, expressed by the eigenvalue separation between the leading and second SPOD modes. This shows that the most energetic, coherent structures that characterize the leading SPOD mode are less dominant with respect to suboptimal modes. Zero-frequency streaky structures associated with helical wave numbers $m = 1-4$ are globally the most affected by the flight stream, on account of both their energy attenuation and spatial distortion (see Figs. 21 and 23).

Throughout the study, a normalized coordinate, x/x_c , based on the potential core length is used to make careful comparisons between the static and flight cases at different streamwise positions. This normalization, which attempts to account for the mean-flow stretching, reveals some similarities in important flow properties. For instance, the centerline velocity profiles collapse when plotted as a function of the scaled streamwise coordinate, and the azimuthal organization of energy in the two cases also scales, to a great extent, with x_c . Furthermore, a stretching parameter, A , defined as the ratio of potential core lengths was shown to successfully correct the modifications in spatial growth rates of the Kelvin-Helmholtz instability in the static and flight cases. The scaled growth rates, $\alpha_i \delta_\theta A$, are shown to collapse when plotted as a function of scaled frequencies, $St \delta_\theta (1/A)$. The scaled frequency of the most amplified mode, $St_{\max} \delta_\theta (1/A)$, is also seen to be the same in static and flight conditions. Global SPOD performed on the LES data showed that low-frequency streaky structures associated with helical wave numbers are the most distorted by the flight stream. Such distortion is not simply an effect of the potential core stretching, as evidenced by the low values of the β metric shown in Fig. 23. Such metric measures the alignment between SPOD modes of the static and flight cases, taking into account the mean flow scaling by x_c . At KH-dominated frequencies, however, β

is significantly higher, showing that the spatial organization of KH wavapackets, unlike that of Orr and streaky structures, is largely established by the potential core length.

The most salient modifications on the energy spectrum are found to be well-captured by results of a locally parallel model, based on the difference in the mean flows of the two jets. The attenuation of KH wavepackets and streaky structures are predicted by eigen- and resolvent analysis, respectively. Stabilization of the KH mechanism is consistent with the weakening of the leading SPOD mode in the range $0.4 \leq St \leq 0.8$ with respect to suboptimal modes, showing a deterioration of the low-rank behavior of the jet in that zone. Moreover, resolvent analysis also predicts a reduction between the optimal gains, σ_1 and those of suboptimal modes at different m in the near-nozzle region, consistent with the reduction in eigenvalue separation at $St \rightarrow 0$ (see Fig. 9). These results show that, despite the fully developed turbulence and the high Reynolds number, the changes in the flow dynamics produced by the flight stream are due, to a great extent, to a linear mean-flow effect rather than a more complex, nonlinear reorganization of the flow.

Overall, the results of the present study show that the reduction in turbulent kinetic energy produced by the flight stream, and frequently evoked in the literature [34], is largely underpinned by the weakening of different categories of coherent structures. Coherent structures are widely considered to underpin sound generation in jets, and therefore their attenuation is expected to be associated with the broadband changes in the acoustic spectra shown in Fig. 1. In this sense, the results reported here may be considered as a departure point for a deeper analysis of how associated sound-source mechanisms are impacted by the flight stream. However, educing and modeling sound-source mechanisms in a turbulent jet is an exceptionally delicate and complex task, given the acoustic inefficiency of the flow fluctuations that drive the sound field [79], and is beyond the scope of this work. Future work will address implications of these results for sound radiation. Among other aspects, it is worth studying how the reorganization of energy in the frequency-wave-number space affects the sound directivity associated with different coherent structures, or how the dynamics of such structures is impacted by a flight stream if shear is held constant.

ACKNOWLEDGMENTS

The authors would like to thank Damien Eysseric for his invaluable work during the PIV measurements. The authors also acknowledge Drs. Matteo Mancinelli, Eduardo Martini, Petrônio Nogueira and Bruno Zebrowski for helpful discussions and insights concerning the mean-flow model. This work has received funding from the Clean Sky 2 Joint Undertaking (JU) under the European Union's Horizon 2020 research and innovation programme under Grant Agreement No. No 785303. Results reflect only the authors' view and the JU is not responsible for any use that may be made of the information it contains. The LES studies performed at Cascade were supported in part by NAVAIR SBIR project with computational resources provided by DoD HPCMP. I.A.M. also acknowledges support from the Science Without Borders program through the CNPq Grant No. 200676/2015-6.

APPENDIX A: AZIMUTHAL NORMALIZATION OF SPOD ENERGY MAPS

An alternative way of looking at the SPOD energy maps is obtained by normalizing the modal energy at each (St, m) pair by the sum of energy across all wave numbers, $\sum_m \lambda_1(m, St)$,

$$\tilde{\lambda}_1 = \lambda_1(m, St) / \sum_m \lambda_1(m, St), \quad (\text{A1})$$

as proposed by Pickering *et al.* [32]. This metric, shown in Fig. 24, provides a more direct indication of the most energetic azimuthal wave number at each St . Close to the nozzle exit, helical modes (underpinned by the lift-up mechanism) are clearly dominant. As the jet evolves downstream, $m = 0$

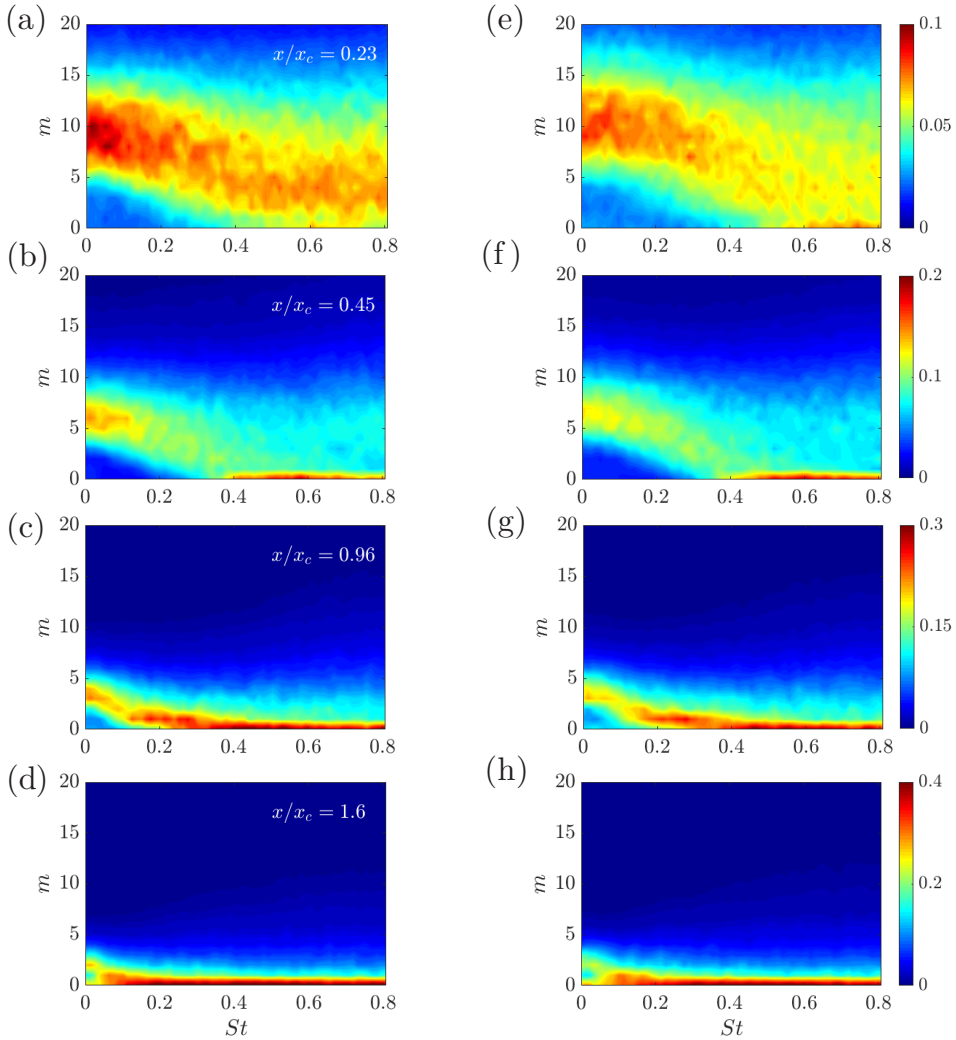


FIG. 24. Modal energy maps of the leading SPOD mode in the St - m plane for different streamwise positions based on PIV data. Modal energy is normalized by the sum of energy across azimuthal modes $\sum_m \lambda_1(m, St)$ for each Strouhal number. (a)–(d) Maps for the $M_f = 0$ case; (e)–(h) maps for the $M_f = 0.15$ case.

Kelvin-Helmholtz wavepackets grow exponentially and dominate the spectrum at $St \geq 0.4$. This is seen here more clearly than in Fig. 9. Further downstream, mode $m = 1$ becomes important in a broad range of Strouhal numbers, and the Orr mechanism also starts to leave its signature at low Strouhal numbers. However, in the limit $St \rightarrow 0$, the streak mechanism ($m > 0$) is always the dominant one. When normalized this way, the energy maps for the two jets were found to display a very similar organization over an extensive streamwise range. At the very initial jet region, represented here by the plots at $x/x_c = 0.23$, it can be seen, however, that the $M_f = 0.15$ case has a broader spectrum in the m direction. But the discrepancy with respect to the baseline case diminishes with increasing streamwise distance, and the maps for both jets are globally very much alike.

APPENDIX B: LINEARIZED NAVIER-STOKES EQUATIONS WITH A LOCALLY PARALLEL ASSUMPTION

The point of departure is the compressible Navier-Stokes equations:

$$\frac{\partial \rho}{\partial t} + \bar{\nabla} \cdot (\rho \mathbf{u}), \quad (\text{B1})$$

$$\rho \left[\frac{\partial \mathbf{u}}{\partial t} + \mathbf{u} \cdot \bar{\nabla} \mathbf{u} \right] = -\bar{\nabla} p + \bar{\nabla} \cdot \left[\left(\beta - \frac{2}{3} \mu \right) \bar{\nabla} \cdot \mathbf{u} \right] + \bar{\nabla} \cdot [\mu (\bar{\nabla} \mathbf{u} + (\bar{\nabla} \mathbf{u})^T)], \quad (\text{B2})$$

$$\rho C_v \left[\frac{\partial T}{\partial t} + \mathbf{u} \cdot \bar{\nabla} T \right] = -\rho \bar{\nabla} \cdot \mathbf{u} + \Phi + k \nabla^2 T, \quad (\text{B3})$$

complemented by the state equation for an ideal gas. β is the bulk viscosity, C_v is the specific heat at constant volume and k is the fluid thermal conductivity. For the sake of simplicity, we set $\beta = 0$. Furthermore, since the jets under study here are isothermal, temperature gradients are negligible and the viscosity, μ was assumed to be constant throughout the domain. The energy dissipation term, Φ , is given by

$$\Phi = \left[\left(\beta - \frac{2}{3} \mu \right) \bar{\nabla} \cdot \mathbf{u} + \mu (\bar{\nabla} \mathbf{u} + (\bar{\nabla} \mathbf{u})^T) \right] [\mu (\bar{\nabla} \mathbf{u} + (\bar{\nabla} \mathbf{u})^T)]. \quad (\text{B4})$$

The variables are then normalized using jet quantities: $\mathbf{u}^+ = \mathbf{u}/U_j$, $p^+ = p/(\rho_j U_j^2)$, $T^+ = T/T_j$, $\rho^+ = \rho/\rho_j$, $t^+ = tU_j/D$, $\mathbf{x}^+ = \mathbf{x}/D$. For the linearization of Eqs. (B1)–(B3), flow variables are decomposed into a mean and a fluctuation component,

$$\mathbf{q}(x, r, \theta, t) = \bar{\mathbf{q}}(x, r, \theta) + \mathbf{q}'(x, r, \theta, t). \quad (\text{B5})$$

Under the assumption of parallel flow, all streamwise derivatives of mean quantities are neglected, $\partial(\bar{\cdot})/\partial x = 0$. Using the axisymmetry of the jet, we can also set $\bar{\mathbf{u}} = [\bar{U}_x(r), \bar{U}_r = 0, \bar{U}_\theta = 0]$, $\bar{\rho} = \bar{\rho}(r)$ and $\bar{T} = \bar{T}(r)$. After all the simplifications, substitution of the *Ansatz* in Eq. (6) into the linearized equations leads to the following relation:

$$-i\omega \begin{bmatrix} \hat{\rho} \\ \hat{u}_x \\ \hat{u}_r \\ \hat{u}_\theta \\ \hat{T} \end{bmatrix} + (\mathcal{A}_0 + \alpha \mathcal{A}_1 + \alpha^2 \mathcal{A}_2) \bar{\mathbf{q}} \begin{bmatrix} \hat{\rho} \\ \hat{u}_x \\ \hat{u}_r \\ \hat{u}_\theta \\ \hat{T} \end{bmatrix} = \mathbf{f}. \quad (\text{B6})$$

The operators \mathcal{A}_0 , \mathcal{A}_1 and \mathcal{A}_2 , which compose the term $\mathcal{A}_{\mathbf{q}, \alpha, m}$ in Eq. (9), are

$$\mathcal{A}_0 = \begin{bmatrix} 0 & 0 & \partial_r \bar{\rho} + \bar{\rho} (\mathbf{D}_{r1} + \frac{1}{r}) & \bar{\rho} \frac{im}{r} & 0 \\ 0 & -\frac{1}{\text{Re}} [\mathbf{D}_{r2} + \frac{1}{r} \mathbf{D}_{r1} - \frac{m^2}{r^2}] & \bar{\rho} \partial_r \bar{U}_x & 0 & 0 \\ -\frac{T}{\gamma M_j^2} \mathbf{D}_{r1} + \frac{1}{\gamma M_j^2} \partial_r \bar{T} & 0 & \frac{1}{\text{Re}} \left[-\frac{4}{3} \left(\mathbf{D}_{r2} + \frac{1}{r} \mathbf{D}_{r1} - \frac{m^2}{r^2} \right) \right] & \frac{im}{3\text{Re}} \left[-\mathbf{D}_{r1} + \frac{7}{r} \right] & \frac{T}{\gamma M_j^2} \mathbf{D}_{r1} + \frac{1}{\gamma M_j^2} \partial_r \bar{\rho} \\ \frac{im\bar{T}}{\gamma M_j^2 r} & 0 & -\frac{1}{3\text{Re}} \frac{im}{r} \left[\mathbf{D}_{r1} + \frac{7}{r} \right] & \frac{1}{\text{Re}} \left[\frac{4}{3} \frac{m^2}{r^2} - \mathbf{D}_{r2} - \frac{1}{r} \mathbf{D}_{r1} + \frac{1}{r^2} \right] & \frac{im\bar{\rho}}{r\gamma M_j^2} \\ 0 & -\frac{2M_j \gamma (\gamma - 1)}{\text{Re}} \partial_r \bar{U}_x \mathbf{D}_{r1} & \bar{\rho} \partial_r \bar{T} + \bar{\rho} (\gamma - 1) \bar{T} (\mathbf{D}_{r1} + \frac{1}{r}) + \partial_r \bar{T} & \bar{\rho} (\gamma - 1) \bar{T} \frac{im}{r} & -\frac{\gamma}{\text{RePr}} \left[\mathbf{D}_{r2} + \frac{1}{r} \mathbf{D}_{r1} + \frac{m^2}{r^2} \right] \end{bmatrix}, \quad (\text{B7})$$

$$\mathcal{A}_1 = \begin{bmatrix} i\bar{U}_x & i\bar{\rho} & 0 & 0 & 0 \\ i\frac{\bar{T}}{\gamma M_j^2} & i\bar{\rho} \bar{U}_x & -\frac{1}{3\text{Re}} \left[i\mathbf{D}_{r1} + \frac{1}{r} \right] & \frac{1}{\text{Re}} \left[-\frac{2}{3} \frac{m^2}{r^2} + \frac{m}{r} \right] & \frac{i\bar{\rho}}{M_j^2} \\ 0 & -\frac{1}{3\text{Re}} i\mathbf{D}_{r1} & i\bar{\rho} \bar{U}_x & 0 & 0 \\ 0 & \frac{1}{3\text{Re}} \frac{m}{r} & 0 & i\bar{\rho} \bar{U}_x & 0 \\ 0 & i\bar{\rho} (\gamma - 1) \bar{T} & -\frac{2iM_j \gamma (\gamma - 1)}{\text{Re}} \partial_r \bar{U}_x & 0 & i\bar{\rho} \bar{U}_x \end{bmatrix}, \quad (\text{B8})$$

$$\mathcal{A}_2 = \begin{bmatrix} 0 & 0 & 0 & 0 & 0 \\ \frac{4}{3\text{Re}} & 0 & 0 & 0 & 0 \\ 0 & 0 & \frac{1}{\text{Re}} & 0 & 0 \\ 0 & 0 & 0 & \frac{1}{\text{Re}} & 0 \\ 0 & 0 & 0 & 0 & \frac{\gamma}{\text{RePr}} \end{bmatrix}, \quad (\text{B9})$$

where Pr is the Prandtl number, which is taken as 0.7, and $\gamma = 1.4$ is the specific heat ration. The superscripts $+$ have been dropped for simplicity. \mathbf{D}_{r_1} , \mathbf{D}_{r_2} are the first- and second-order Chebyshev derivation matrices. $\partial_r(\bar{\cdot})$ denotes the radial derivative of the mean field. As mentioned in Sec. VII, for the resolvent analysis, the molecular Reynolds number, Re is later replaced by a turbulent Reynolds number, Re_T . Each element of A_0 , A_1 , A_2 is a $N \times N$ matrix, where N is the number of Chebyshev points used. We found that 600 points were sufficient to attain converged results. The observation and forcing restrictions matrices, \mathcal{C} and \mathcal{B} , respectively, in Eq. (9), are equal to the identity matrix of dimension $5N \times 5N$. Dirichlet boundary conditions were applied in the far-field, $r/D \rightarrow \infty$. At the jet centerline, $r/D = 0$, following Khorrami *et al.* [80] and Lesshafft and Huerre [64] the following symmetry boundary conditions were imposed:

$$\left. \begin{array}{l} \frac{\partial \hat{\rho}}{\partial r} = 0 \\ \frac{\partial \hat{u}_x}{\partial r} = 0 \\ \hat{u}_r = 0 \\ \hat{u}_\theta = 0 \\ \frac{\partial \hat{T}}{\partial r} = 0 \end{array} \right\} \text{ for } m = 0, \quad (\text{B10})$$

$$\left. \begin{array}{l} \hat{\rho} = 0 \\ \hat{u}_x = 0 \\ \frac{\partial \hat{u}_r}{\partial r} = 0 \\ \hat{u}_r + i\hat{u}_\theta = 0 \\ \hat{T} = 0 \end{array} \right\} \text{ for } m = 1, \quad (\text{B11})$$

$$\left. \begin{array}{l} \hat{\rho} = 0 \\ \hat{u}_x = 0 \\ \hat{u}_r = 0 \\ \hat{u}_\theta = 0 \\ \hat{T} = 0 \end{array} \right\} \text{ for } m \geq 2, \quad (\text{B12})$$

where the conditions for $\hat{\rho}$ and \hat{T} for $m = 0$ were derived assuming \hat{u}_r to be an odd function of r .

-
- [1] A. K. M. F. Hussain, Coherent structures and turbulence, *J. Fluid Mech.* **173**, 303 (1986).
 - [2] G. L. Brown and A. Roshko, On density effects and large structure in turbulent mixing layers, *J. Fluid Mech.* **64**, 775 (1974).
 - [3] E. Mollo-Christensen, Jet noise and shear flow instability seen from an experimenter's viewpoint, *J. Appl. Mech.* **34**, 1 (1967).
 - [4] S. Crow and F. Champagne, Orderly structure in jet turbulence, *J. Fluid Mech.* **48**, 547 (1971).
 - [5] C. J. Moore, The role of shear-layer instability waves in jet exhaust noise, *J. Fluid Mech.* **80**, 321 (1977).
 - [6] K. B. M. Q. Zaman and A. K. M. F. Hussain, Vortex pairing in a circular jet under controlled excitation. Part 1. General jet response, *J. Fluid Mech.* **101**, 449 (1980).
 - [7] A. K. M. F. Hussain and K. B. M. Q. Zaman, Vortex pairing in a circular jet under controlled excitation. Part 2. Coherent structure dynamics, *J. Fluid Mech.* **101**, 493 (1980).

- [8] A. K. M. F. Hussain and K. B. M. Q. Zaman, The “preferred” mode of the axisymmetric jet, *J. Fluid Mech.* **110**, 39 (1981).
- [9] R. A. Petersen and M. M. Samet, On the preferred mode of jet instability, *J. Fluid Mech.* **194**, 153 (1988).
- [10] J. L. Lumley, The structure of inhomogeneous turbulent flows, in *Atmospheric Turbulence and Radio Wave Propagation*, edited by A. M. Yaglom and V. I. Tartarsky (Nauka, Moscow, 1967), pp. 166–177.
- [11] T. Suzuki and T. Colonius, Instability waves in a subsonic round jet detected using a near-field phased microphone array, *J. Fluid Mech.* **565**, 197 (2006).
- [12] K. Gudmundsson and T. Colonius, Instability wave models for the near-field fluctuations of turbulent jets, *J. Fluid Mech.* **689**, 97 (2011).
- [13] D. E. S. Breakey, P. Jordan, A. V. G. Cavalieri, P. A. Nogueira, O. Léon, T. Colonius, and D. Rodríguez, Experimental study of turbulent-jet wave packets and their acoustic efficiency, *Phys. Rev. Fluids* **2**, 124601 (2017).
- [14] A. V. G. Cavalieri, D. Rodríguez, P. Jordan, T. Colonius, and Y. Gervais, Wavepackets in the velocity field of turbulent jets, *J. Fluid Mech.* **730**, 559 (2013).
- [15] V. Jaunet, P. Jordan, and A. V. G. Cavalieri, Two-point coherence of wavepackets in turbulent jets, *Phys. Rev. Fluids* **2**, 024604 (2017).
- [16] K. Sasaki, A. V. G. Cavalieri, P. Jordan, O. T. Schmidt, T. Colonius, and G. A. Brès, High-frequency wavepackets in turbulent jets, *J. Fluid Mech.* **830**, R2 (2017).
- [17] W. Orr, The stability or instability of steady motions of a perfect liquid and of a viscous liquid. Part I: A perfect liquid, *Proc. Royal Irish Acad. Sec. A: Math. Phys. Sci.* **27**, 9 (1907).
- [18] L. Brandt, The lift-up effect: The linear mechanism behind transition and turbulence in shear flows, *Eur. J. Mech. B Fluids* **47**, 80 (2014).
- [19] J. Jiménez, Coherent structures in wall-bounded turbulence, *J. Fluid Mech.* **842**, P1 (2018).
- [20] H. A. Becker and T. A. Massaro, Vortex evolution in a round jet, *J. Fluid Mech.* **31**, 435 (1968).
- [21] F. K. Browand and J. Laufer, The roles of large scale structures in the initial development of circular jets, in *4th Biennial Symposium on Turbulence in Liquids*, University of Missouri-Rolla (Rolla, MO, 1975).
- [22] P. E. Dimotakis, R. C. Miake-Lye, and D. A. Papantoniou, Structure and dynamics of round turbulent jets, *Phys. Fluids* **26**, 3185 (1983).
- [23] A. J. Yule, Large-scale structure in the mixing layer of a round jet, *J. Fluid Mech.* **89**, 413 (1978).
- [24] J. C. Agüí and L. Hesselink, Flow visualization and numerical analysis of a coflowing jet: A three-dimensional approach, *J. Fluid Mech.* **191**, 19 (1988).
- [25] X. Garnaud, L. Lesshafft, P. Schmid, and P. Huerre, The preferred mode of incompressible jets: Linear frequency response analysis, *J. Fluid Mech.* **716**, 189 (2013).
- [26] J. Jeun, J. W. Nichols, and M. R. Jovanovic, Input-output analysis of high-speed axisymmetric isothermal jet noise, *Phys. Fluids* **28**, 047101 (2016).
- [27] O. Semeraro, V. Jaunet, P. Jordan, A. V. G. Cavalieri, and L. Lesshafft, Stochastic and harmonic optimal forcing in subsonic jets, in *Proceedings of the 22nd AIAA/CEAS Aeroacoustics Conference, Lyon, France* (AIAA, Reston, VA, 2016).
- [28] G. Tissot Jr., M. Zhang, F. C. Lajús Jr., A. V. G. Cavalieri, and P. Jordan, Sensitivity of wavepackets in jets to nonlinear effects: The role of the critical layer, *J. Fluid Mech.* **811**, 95 (2017).
- [29] O. T. Schmidt, A. Towne, G. Rigas, T. Colonius, and G. A. Brès, Spectral analysis of jet turbulence, *J. Fluid Mech.* **855**, 953 (2018).
- [30] L. Lesshafft, O. Semeraro, V. Jaunet, A. V. G. Cavalieri, and P. Jordan, Resolvent-based modeling of coherent structures wave packets in a turbulent jet, *Phys. Rev. Fluids* **4**, 063901 (2019).
- [31] P. Nogueira, A. V. G. Cavalieri, P. Jordan, and V. Jaunet, Large-scale streaky structures in turbulent jets, *J. Fluid Mech.* **873**, 211 (2019).
- [32] E. Pickering, G. Rigas, P. Nogueira, A. V. G. Cavalieri, O. Schmidt, and T. Colonius, Lift-up, Kelvin-Helmholtz and Orr mechanisms in turbulent jets, *J. Fluid Mech.* **896**, A2 (2020).
- [33] P. Jordan and T. Colonius, Wave packets and turbulent jet noise, *Annu. Rev. Fluid Mech.* **45**, 173 (2013).
- [34] H. Tanna and P. Morris, In-flight simulation experiments on turbulent jet mixing noise, *J. Sound Vib.* **53**, 389 (1977).

- [35] A. Michalke and G. Hermann, On the inviscid instability of a circular jet with external flow, *J. Fluid Mech.* **114**, 343 (1982).
- [36] L. F. Soares, A. V. G. Cavalieri, V. Kopiev, and G. Faranosov, Flight effects on turbulent-jet wave packets, *AIAA J.* **58**, 3877 (2020).
- [37] X. Garnaud, R. D. Sandberg, and L. Lesshafft, Global response to forcing in a subsonic jet: instability wavepackets and acoustic radiation, in *Proceedings of the 19th AIAA/CEAS Aeroacoustics Conference* (AIAA, Reston, VA, 2013).
- [38] U. Von Glahn, D. Groesbeck, and J. Goodykoontz, Velocity decay and acoustic characteristics of various nozzle geometries with forward velocity, in *Proceedings of the 6th Fluid and Plasma Dynamics Conference* (AIAA, Reston, VA, 1973).
- [39] B. Cocking and W. Bryce, Subsonic jet noise in flight based on some recent wind-tunnel tests, in *Proceedings of the 2nd Aeroacoustics Conference* (AIAA, Reston, VA, 1975).
- [40] K. Bushell, Measurement and prediction of jet noise in flight, in *Proceedings of the 2nd Aeroacoustics Conference* (AIAA, Reston, VA, 1975).
- [41] A. B. Packman, K. W. Ng, and R. W. Paterson, Effect of simulated forward flight on subsonic jet exhaust noise, *J. Aircr.* **13**, 1007 (1976).
- [42] H. E. Plumblee, Effects of forward flight on turbulent jet mixing noise, Technical Report CR-2702, NASA (1976).
- [43] W. Bryce, The prediction of static-to-flight changes in jet noise, in *Proceedings of the 9th Aeroacoustics Conference* (AIAA, Reston, VA, 1984).
- [44] C. L. Morfey and B. J. Tester, Noise measurements in a free jet flight simulation facility: Shear-layer refraction and facility-to-flight corrections, *J. Sound Vib.* **54**, 83 (1977).
- [45] K. Vishwanathan and M. Czech, Measurement and modeling of effect of forward flight on jet noise, *AIAA J.* **49**, 1 (2011).
- [46] A. V. G. Cavalieri, P. Jordan, A. Agarwal, and Y. Gervais, Jittering wave-packet models for subsonic jet noise, *J. Sound Vib.* **330**, 4474 (2011).
- [47] A. V. G. Cavalieri, P. Jordan, T. Colonius, and Y. Gervais, Axisymmetric superdirectivity in subsonic jets, *J. Fluid Mech.* **704**, 388 (2012).
- [48] I. A. Maia, P. Jordan, A. V. G. Cavalieri, and V. Jaunet, Two-point wavepacket modeling of jet noise, *Proc. R. Soc. A* **475**, 20190199 (2019).
- [49] M. J. Lighthill, On sound generated aerodynamically. I. General theory, *Proc. Roy. Soc. London A: Math., Phys. Eng. Sci.* **211**, 564 (1952).
- [50] G. A. Brès, F. E. Ham, J. W. Nichols, and S. K. Lele, Unstructured large eddy simulations of supersonic jets, *AIAA J.* **55**, 1164 (2017).
- [51] G. A. Brès, P. Jordan, V. Jaunet, M. Le Rallic, A. V. G. Cavalieri, A. Towne, S. K. Lele, T. Colonius, and O. T. Schmidt, Importance of the nozzle-exit boundary-layer state in subsonic turbulent jets, *J. Fluid Mech.* **851**, 83 (2018).
- [52] F. Scarano, Iterative image deformation methods in PIV, *Meas. Sci. Technol.* **13**, R1 (2002).
- [53] J. B. Freund, Proposed inflow/outflow boundary condition for direct computation of aerodynamic sound, *AIAA J.* **35**, 740 (1997).
- [54] A. Mani, Analysis and optimization of numerical sponge layers as a nonreflective boundary treatment, *J. Comput. Phys.* **231**, 704 (2012).
- [55] A. Vreman, An eddy-viscosity subgrid-scale model for turbulent shear flow: Algebraic theory and applications, *Phys. Fluids* **16**, 3670 (2004).
- [56] S. Kawai and J. Larsson, Wall-modeling in large eddy simulation: Length scales, grid resolution, and accuracy, *Phys. Fluids* **24**, 015105 (2012).
- [57] J. Bodart and J. Larsson, Wall-modeled large eddy simulation in complex geometries with application to high-lift devices, in *Annual Research Briefs 2011* (Cent. Turbul. Res., Stanford, CA, 2011), pp. 37–48.
- [58] O. Kaplan, P. Jordan, A. V. G. Cavalieri, and G. Brès, Nozzle dynamics and wavepackets in turbulent jets, *J. Fluid Mech.* **923**, A22 (2021).
- [59] A. Michalke and U. Michel, Prediction of jet noise in flight from static tests, *J. Sound Vib.* **67**, 341 (1979).

- [60] J. H. Citriniti and W. K. George, Reconstruction of the global velocity field in the axisymmetric mixing layer utilizing the proper orthogonal decomposition, *J. Fluid Mech.* **418**, 137 (2000).
- [61] D. Jung, S. Gamard, and W. K. George, Downstream evolution of the most energetic modes in a turbulent axisymmetric jet at high Reynolds number. Part 1. The near-field region, *J. Fluid Mech.* **514**, 173 (1999).
- [62] B. J. McKeon and A. S. Sharma, A critical-layer framework for turbulent pipe flow, *J. Fluid Mech.* **658**, 336 (2010).
- [63] D. Rodríguez, A. V. G. Cavalieri, T. Colonius, and P. Jordan, A study of wavepacket models for subsonic turbulent jets using local ingemod decomposition of PIV data, *Eur. J. Mech. B Fluids* **49**, 308 (2015).
- [64] L. Lesshafft and P. Huerre, Linear impulse response in hot round jets, *Phys. Fluids* **19**, 024102 (2007).
- [65] G. Dergham, D. Sipp, and J-Ch. Robinet, Stochastic dynamics and model reduction of amplifier flows: The backward facing step, *J. Fluid Mech.* **719**, 406 (2013).
- [66] P. Nogueira, A. V. G. Cavalieri, A. Hanifi, and D. S. Henningson, Resolvent analysis in unbounded flows: The role of free-stream modes, *Theor. Comput. Fluid Dyn.* **34**, 163 (2020).
- [67] J. D. Crouch, A. Garbaruk, and D. Magidov, Predicting the onset of flow unsteadiness based on global instability, *J. Comput. Phys.* **224**, 924 (2007).
- [68] K. Oberleithner, C. O. Paschereit, and I. Wygnanski, On the impact of swirl on the growth of coherent structures, *J. Fluid Mech.* **741**, 156 (2014).
- [69] L. Rukes, O. Paschereit, and K. Oberleithner, An assessment of turbulence models for linear hydrodynamic stability analysis of strongly swirling jets, *Eur. J. Mech. B Fluids* **59**, 205 (2016).
- [70] O. Tammisola and M. P. Juniper, Coherent structures in a swirl injector at $Re = 4800$ by nonlinear simulations and linear global modes, *J. Fluid Mech.* **792**, 620 (2016).
- [71] G. Y. Hwang and C. Cossu, Amplification of coherent streaks in the turbulent Couette flow: An input-output analysis at low Reynolds number, *J. Fluid Mech.* **643**, 333 (2010).
- [72] P. Morra, O. Semeraro, D. S. Henningson, and C. Cossu, On the relevance of Reynolds stresses in resolvent analyses of turbulent wall-bounded flows, *J. Fluid Mech.* **867**, 969 (2019).
- [73] E. Pickering, G. Rigas, O. T. Schmidt, D. Sipp, and T. Colonius, Optimal eddy-viscosity models of coherent structures in turbulent jet, *J. Fluid Mech.* **917**, A29 (2021).
- [74] P. Kuhn, J. Soria, and K. Oberleithner, Linear modeling of self-similar jet turbulence, *J. Fluid Mech.* **919**, A7 (2021).
- [75] B.-T. Chu, On the energy transfer to small scale disturbances in fluid flow (part 1), *Acta Mech.* **1**, 215 (1965).
- [76] E. Åkervik, U. Ehrenstein, F. Gallaire, and D. S. Henningson, Global two-dimensional stability measures of the flat plate boundary-layer flow, *Eur. J. Mech. B Fluids* **27**, 501 (2008).
- [77] C. Arratia, C. P. Caulfield, and J.-M. Chomaz, Transient perturbation growth in time-dependent mixing layers, *J. Fluid Mech.* **717**, 90 (2013).
- [78] M. J. P. Hack and P. Moin, Algebraic disturbance growth by interaction of Orr and lift-up mechanisms, *J. Fluid Mech.* **829**, 112 (2017).
- [79] U. Karban, B. Bugeat, A. Towne, L. Lesshafft, A. Agarwal, and P. Jordan, An empirical model of noise sources in subsonic jets, [arXiv:2210.01866](https://arxiv.org/abs/2210.01866).
- [80] M. R. Khorrami, M. R. Malik, and R. L. Ash, Applications of spectral collocation techniques to the stability of swirling flows, *J. Comput. Phys.* **81**, 206 (1989).